Sensorimotor Integration Supporting Perception Requires *Syngap1* Expression in Cortex

Thomas Vaissiere[1*], Sheldon Michaelson[1*], Thomas Creson[1], Jessie Goins[1], Daniel Fürth[2], Diana Balazsfi[1], Camilo Rojas[1], Randall Golovin[1], Konstantinos Meletis[3], Courtney A. Miller[1,4], Daniel O'Connor[5], and Gavin Rumbaugh[1#]

[1]Department of Neuroscience, The Herbert Wertheim UF Scripps Institute for Biomedical Innovation & Technology, Jupiter, FL, USA
[2]SciLifeLab, Department of Immunology, Genetics & Pathology, Uppsala University, Uppsala, Sweden
[3]Department of Neuroscience, Karolinska Institute, 17177 Stockholm, Sweden
[4]Department of Molecular Medicine, UF Scripps Biomedical Research, Jupiter, FL, USA
[5]Department of Neuroscience, The Johns Hopkins University School of Medicine, Baltimore, MD, USA
**Equal Contribution*

[#]Correspondence: Gavin Rumbaugh, PhD
Department of Neuroscience
The Herbert Wertheim UF Scripps Institute for Biomedical Innovation & Technology
120 Scripps Way, #3B3
Jupiter, FL 33458
gavinrumbaugh@ufl.edu
https://rumbaugh.scripps.ufl.edu/

Summary

Perception, a cognitive construct, emerges through sensorimotor integration (SMI). The molecular and cellular mechanisms that shape SMI within circuits that promote cognition are poorly understood. Here, we demonstrate that expression of the autism/intellectual disability gene, *Syngap1*, in mouse cortical excitatory neurons promotes touch sensitivity required to elicit perceptual behaviors. Cortical *Syngap1* expression enabled touch-induced feedback signals within sensorimotor loops by assembling circuits that support tactile sensitivity. These circuits also encoded correlates of attention that promoted self-generated whisker movements underlying purposeful and sustained object exploration. As *Syngap1* deficient animals explored objects with whiskers, relatively weak touch signals were integrated with relatively strong motor signals. This produced a signal-to-noise deficit consistent with impaired tactile sensitivity, reduced tactile exploration, and weak tactile learning. Thus, *Syngap1* expression in cortex promotes tactile perception by assembling circuits that integrate touch and whisker motor signals. Deficient *Syngap1* expression likely contributes to cognitive impairment through abnormal top-down SMI.

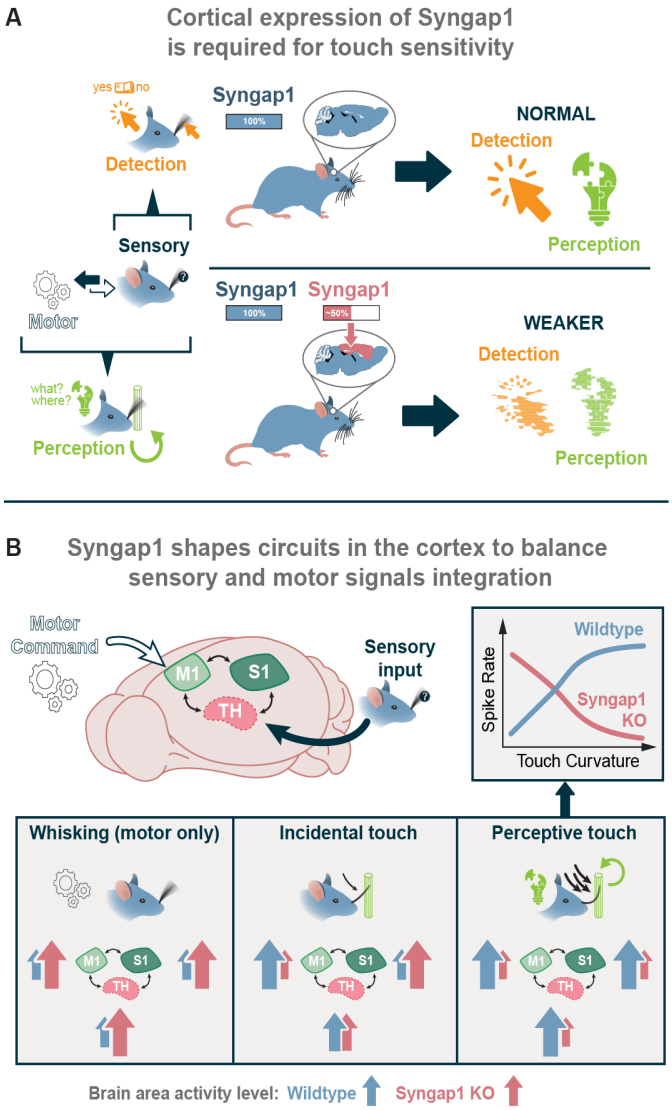

Introduction

Sensorimotor integration (SMI) refers to the neurophysiological phenomenon reflecting how sensory processing and motor output influence each other[1,2]. SMI is essential to a range of motor and higher cognitive functions, from posture, balance and movement control to attention, memory, and learning[3–7]. Sensory and motor signals are conveyed across multiple time scales through distributed networks and brain areas[5]. In rodents, disrupting SMI impairs neural representations of object features (texture, contour, and relative location), which are required for more complex cognitive functions to emerge, such as sensory perception and salience[8–12]. However, the neurobiological processes that shape the connectivity of distributed SMI networks that promote higher cognitive functions remain unknown. This hinders our understanding of the neural correlates of adaptive behaviors.

In addition to supporting a healthy brain, SMI processes are associated with a diverse range of disease/disorder states. This includes clumsiness, abnormal eye tracking, and altered sensory integration/reactivity, which are core features of neuropsychiatric disorders, such ASD and psychosis, and are also observed as “soft signs” in many neurological disorders [13–18]. Genetic factors in the central and peripheral nervous systems have been implicated in abnormal sensory reactivity and altered motor control [19–23]. Mutations in several genes have been identified in neurodevelopmental disorders (NDD) that feature alterations in sensory processing, motor control, and intellectual ability [24–29]. Impaired SMI could, therefore, be a neural substrate of altered cognitive processes broadly observable in mental health disorders[28,30–33]. However, there have been comparatively few neurobiological investigations into how highly penetrant NDD risk genes contribute to SMI, resulting in a poor understanding of how this essential neural process shapes adaptive behavior in health and disease.

We hypothesized that highly penetrant NDD genes regulate neurophysiological correlates of SMI required for higher cognitive functions. As an initial test of this hypothesis, we chose a relevant NDD gene and then tested how its expression contributed to SMI and associated cognitive functions. We chose *SYNGAP1*/*Syngap1* because expression of this NDD gene in humans and mice, respectively, is required for both sensory processing and motor control [23,34]. Indeed, *de novo* mutations that lower *SYNGAP1* expression in humans cause a developmental and epileptic encephalopathy defined by impaired cortical excitability, postural/gait abnormalities, sensory processing impairments, and moderate-to-severe intellectual disability[35–39]. Importantly, excellent mouse genetic tools are available for the study of *Syngap1*. These tools enable region- and/or cell-specific bidirectional regulation of its expression, which allow spatial investigations into how *Syngap1* regulates distributed neural systems associated with SMI. These models have been used to uncover a role for *Syngap1* in cortical processing of sensory signals and control of motor responses required for decision-making [23,40,41]. However, it remains unknown if *Syngap1* expression regulates neural correlates of SMI, and if so, how this contributes to constructs of cognition required for behavioral adaptation.

Here, *Syngap1* mouse genetic tools were used to explore how its expression regulates neurobehavioral correlates of SMI associated with constructs of cognition. To explore this, we utilized behavioral paradigms that rely on passive (receptive) and active (generative) whisker sensing to drive perceptual learning [42,43]. In active tasks, tactile feedback enables closed loop, ongoing control of whisker motion, which promotes perception by enabling self-generated control of object exploration during tactile learning [9,44].The structural and functional connectivity of the rodent somatomotor whisker system has been extensively elucidated [30,45–48]. The key nodes in higher-order whisker-related motor-sensory-motor (MSM) loops are known, and paradigms have been established that enable neurophysiological measurements of neuronal populations that mediate motor control during whisking, as well as tactile signals generated during object exploration. Importantly, disrupting self-generated motor control of whiskers during object exploration impairs perceptual learning [49,50]. Thus, simultaneous tracking of whisker movement during object exploration and recording of activity within integrative neuronal populations enables elucidation of neurobiological principles that link SMI to cognition and behavior.

Using this framework, we utilized an array of *Syngap1* mouse models in learning paradigms that require the use of whiskers to generate percepts for behavioral adaptation. We paired these investigations with structural and functional analysis of somatomotor-associated neural circuits that integrate tactile and whisker motor signals. Combining these approaches, we demonstrate that *Syngap1* expression in cortical excitatory neurons is required for perceptual decision-making driven by tactile input, and for tactile-generated feedback control of whisker motion that underlies attention during active sensing. We also demonstrate that *Syngap1* regulates the structural/functional connectivity of cortical circuits within MSM loops known to integrate signals coding for touch and whisker motion. Together, these results demonstrate that a key function of *Syngap1* expression is to promote balanced integration of tactile and whisker motor signals within cortical sensorimotor loops. We propose this form of abnormal SMI within the cortex of *Syngap1* mice contributes to reduced tactile sensitivity, weak perceptual learning, and maladaptive behaviors.

Results

Syngap1 expression promotes whisker touch sensitivity and perceptual learning

We and others have previously demonstrated a role for *Syngap1* in both tactile learning and neural representations of tactile stimuli in somatosensory cortex [23,51,52]. However, this past work did not define if, how, and to what extent, *Syngap1* contributes to tactile learning through sensory processing. To begin to investigate sensory-mediated mechanisms linking *Syngap1* expression to perceptual learning underlying behavioral adaptation, we utilized a variation of a head-fixed tactile detection task where water-restricted animals were trained to provide a

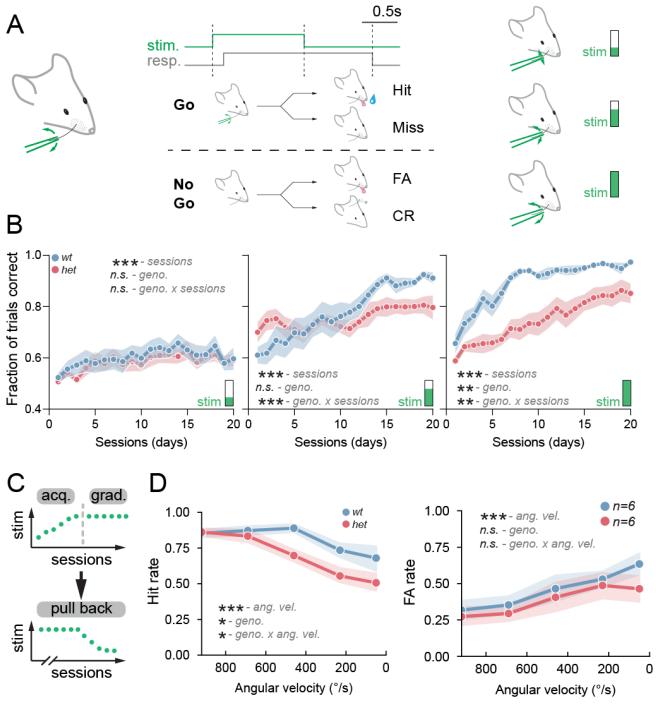

Figure 1. Syngap1 expression promotes perceptual learning (tactile sensitivity) during passive tactile stimulus (WDIL). A. Schematic of detection paradigm through whisker-dependent instrumental learning paradigm (WDIL), including single whisker detection task structure and response outcomes with go trials being discriminated by single whisker deflection for 3 different whisker stimulus intensities (~ 400, 650 and 900 °/s). B. Fraction of total trials correct during WDIL for 3 different whisker stimulus intensities (~ 400, 650 and 900 °/s). C. Summary schematic of the training phase and the reduced stimulation phase. D. False alarm (FA) and hit rates for animals that reached criteria and underwent the reduced stimulation phase (pull back). (wt, blue) and *Syngap1*$^{+/-}$ (het, red); (n.s.: p>0.05, *: p<0.05, **: p<0.01, ***: p<0.001).

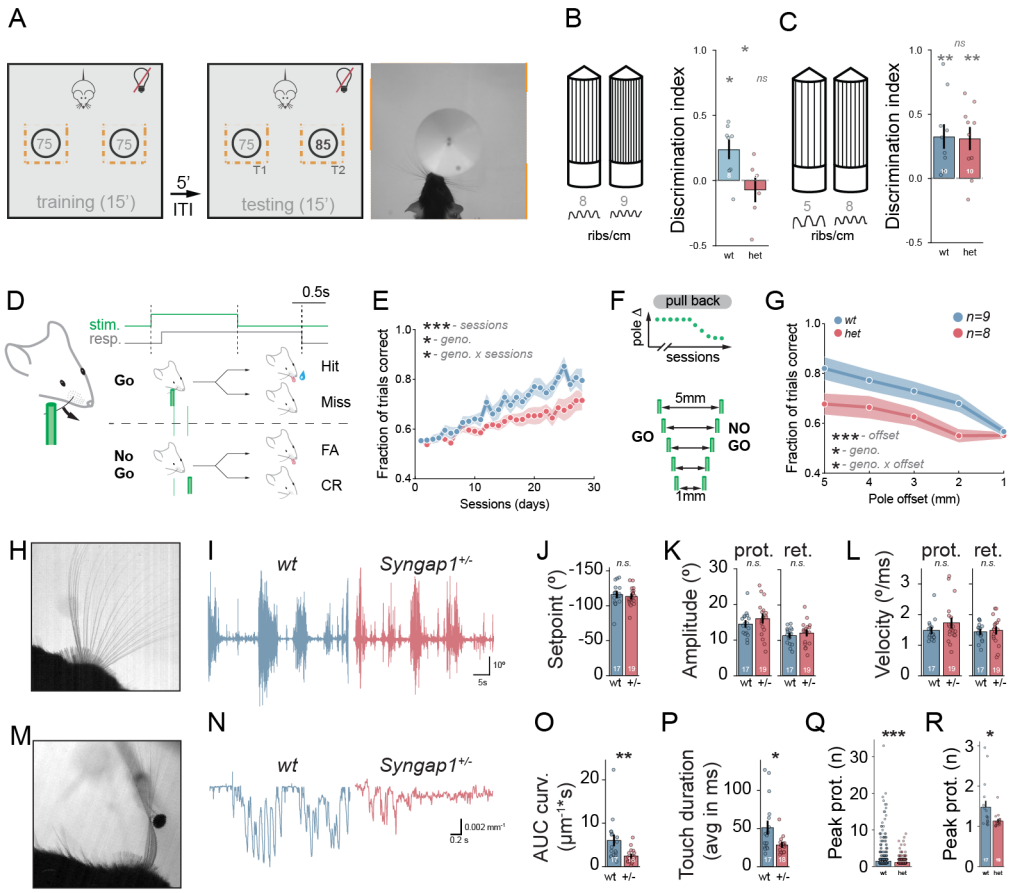

Figure 2. Syngap1 expression promotes perceptual learning (tactile sensitivity) in active sensing paradigms. A-C. Novel object recognition texture (NOR-T) task structure. Discrimination index during the testing phase of the NOR-T for objects with 10 groves spacing difference (B) and 25 groves spacing differences (C). D-G. Whisker-dependent discrimination task during instrumental learning based on pole location. Fraction of total trials correct during the acquisition phase of the pole-location discrimination task (E). Schematic of the reduced stimulation phase of the pole-location discrimination task (F) and fraction of total trials correct for animals that reached criteria and underwent the reduced stimulation phase (pull back). (wt, blue) and *Syngap1*$^{+/-}$ (het, red); n.s.: not significant, *: p<0.05, **: p<0.01, ***: p<0.001). H-L Whisker dynamics in free air and during object exploration. Superimposition of 40 frames representing whisking in wt mouse acquired at 500Hz illustrating free whisking of a single whisker (H). Representative traces of whisker angle in wt (blue) and *Syngap1*$^{+/-}$ (red, i). Quantification of whisker setpoint (J), amplitude (K) and velocity (L) during the protraction (prot.) and retraction (ret.) whisking phase during a 30 second recording window. M-R Active touch dynamics of a single whisker for the first 30 seconds of pole presentation, superimposition of 40 frames representing active touch (M). Representative traces of whisker curvature (N) and quantification of area under the curve (AUC) for whisker curvature (O), average touch duration (P) and the total number of peak protractions detected for each individual touch event (Q) and their respective animal average (R). (wt, blue) and *Syngap1*$^{+/-}$ (het, red); (n.s.: p>0.05, *: p<0.05, **: p<0.01, ***: p<0.001)..

perceptual report of a passive whisker stimulation by licking a sensor that also supplies a water reward **(Figure 1A)**.

Three cohorts of *Syngap1*$^{+/+}$ (WT – normal SynGAP protein expression) and *Syngap1*$^{+/-}$ (germline heterozygous – half SynGAP protein expression) mice were trained, with each cohort receiving either a weak, medium, or strong whisker training stimulus during "Go" trials. Go trials were defined by a piezo deflection that induced a whisker stimulation; an animal scored a "hit" when licking the detector on these trials. "NoGo" trials were defined by a piezo deflection that did not translate into a whisker stimulus; an animal scored a "correct rejection" (CR) by withholding licking during these trials. We evaluated task performance of *Syngap1*$^{+/+}$ and *Syngap1*$^{+/-}$ mice by measuring total correct choices (hit on Go trials; CR on NoGo trials), overall Hit rate, overall False Alarm (FA) rate (FA = licking on a NoGo trial), and a trial discrimination index (*d'*). Stimulus intensity positively correlated with performance in *Syngap1*$^{+/+}$ mice, with faster learning over the 21-day training period with stronger stimulus intensity **(Figure 1B)**, and improved trial discrimination at the end of training in strong versus weak training stimuli **(Figure S1A-O)**. However, *Syngap1* heterozygous mice exhibited deficient learning compared to controls as evidenced by fewer total correct choices, particularly in the strongest training stimulus **(Figure 1B; Table S1).** Additional analysis of trial data revealed that *Syngap1*$^{+/-}$ mice exhibited significancy fewer Hits compared with littermate controls in the medium stimuli paradigm **(Figure S1F-G)**, and fewer hits with more FAs in the strong stimulus experiment **(Figure S1K-I)**. A statistical model that considered all three cohorts revealed that the probability of correct choices in *Syngap1* heterozygous mice was less sensitive to increases in training stimulus intensity **(Table S1-** *all subsequent comparisons are present in this table***)**. This suggested that *Syngap1* mice have reduced tactile sensitivity, though dual Hit and FA impairments could be a consequence of a fundamental disruption to distributed and generalized reinforcement learning mechanisms and/or motor control issues. To definitively determine if *Syngap1*$^{+/-}$ mice exhibit reduced tactile sensitivity, we carried out a "pull-back" experiment [53] where animals that met acquisition criteria were subjected to a daily reduction in Go-stimulus intensity **(Figure 1C)**. This experiment was possible because of a modified 3-step training paradigm that selected for a subset of *Syngap1*$^{+/-}$ mice that learned to the same degree as WT littermates **(Figure S1P-S)**. Thus, when additional *Syngap1*$^{+/-}$ mice were trained and the poor learners excluded from additional in-depth training, trial performance ended up no different between genotypes after 21 days of training **(Figure 1D –** *first data point***).** In this pull-back paradigm, there was an effect of genotype and an interaction between genotype and stimulus intensity in Go trials **(Figure 1D)**. Indeed, in well-trained *Syngap1*$^{+/-}$ mice, Hit rates decreased faster relative to littermate controls as the stimulus intensity was reduced. These head-fixed passive whisker stimulation task data demonstrate that *Syngap1* expression promotes tactile sensitivity.

This task reflects perceptual learning through a passive tactile stimulus. However, animals in the wild, including rodents and humans, most often acquire sensory information through self-generated movement of sense organs[54,55]. Therefore, we sought to determine the extent to which *Syngap1* expression regulated tactile sensitivity and associated perceptual adaptations in active sensing paradigms. First, we employed an active whisker-touch paradigm, **N**ovel **O**bjection **R**ecognition using only **T**exture **(NOR-T)**[23], which was carried out in freely moving animals and was, therefore, ethological in nature. Freely moving mice under IR lighting conditions were tasked with discriminating between two identical objects that only differed in texture **(Figure 2A)**. Trimming whiskers in WT test mice prevented the expected shift in time spent around the novel textured object **(Figure S2A-B)**, confirming the task is whisker-dependent. *Syngap1*$^{+/+}$ mice could discriminate between the two objects, while *Syngap1*$^{+/-}$ mice could not **(Figure 2B, Figure S3A)**. However, when the difference in texture pattern density between the objects was greater (8 vs 5 instead of 9 vs 8 vertical ribs/cm, and presumably more perceptually salient, both genotypes could now discriminate **(Figure 2C, Figure S3B)**. Additional object recognition testing was conducted, which confirmed that poor texture discrimination in *Syngap1*$^{+/-}$ mice was caused by reduced tactile sensitivity rather than a more generalized impairment in brain function and behavior. For exam-

ple, *Syngap1*$^{+/-}$ mice were able to discriminate equally well compared to littermate controls in a traditional novel object recognition task that engages multisensory processes **(Figure S2C-D)**. Together, these data demonstrate that *Syngap1* regulation of tactile sensitivity extends to texture discrimination.

In addition to texture discrimination, mice and rats actively use whiskers to perceive the location of objects relative to their head [8,56,57]. To determine how *Syngap1* contributes to this form of tactile perception, we utilized a head-fixed Go/NoGo object localization task[58]. In this task, mice can use a single whisker to discriminate between two distinct object positions near the head **(Figure 2D)**. Water-restricted animals were trained to discriminate between the Go and NoGo positions over ~28 daily sessions. Correct choices on Go trials (e.g., licking the sensor) were reinforced with a water reward; FAs (licking on NoGo) and misses (no licking on Go) went unrewarded and unpunished. While *Syngap1*$^{+/-}$ mice learned to detect the difference between the two locations, there was an effect of genotype, and an interaction between genotype and sessions, on the fraction of correct choices and in the trial discrimination index, *d'* **(Figure 2E, Figure S2E)**. To determine if impaired learning by mutants in this active tactile exploration task was related to impaired sensitivity to detecting object location, we again performed a pull-back experiment **(Figure 2F, Figure S2F)**. Statistical analysis revealed that performance was not the same between genotypes at the end of training. However, an interaction between genotype and object distance during pull-back sessions was detected in total correct choices **(Figure 2G)**. Consistent with impaired sensitivity (e.g., reduced precision) for detecting object location, the pull-back curve indicated that performance dropped off faster in *Syngap1*$^{+/-}$ mice compared to wildtype littermates.

The motion of the whisker relative to an object is essential for determining object texture and location [8,30,46,48]. Object contact causes whiskers to bend, eliciting torques and forces at the whisker base that are proportional to changes in whisker curvature. Strain within the follicle causes action potentials within trigeminal ganglion neurons. Therefore, reduced sensitivity for texture and location in *Syngap1* mice may be related to abnormal whisker motion during object exploration. To directly test this idea, we used a two-step approach that measured whisker kinematics in the same animals with and without the presence of a stationary pole **(Figure 2H, M)**. Whisker dynamics were recorded using high-speed videography followed by offline location tracking with *WHISK*[58] or DeepLabCut[59] (**Figure S4**, **Video S1**). There was no effect of genotype on the setpoint, maximum range of the whisker cycle, or whisker velocity during free air whisking **(Figure 2I-L, Video S2)**, indicating that *Syngap1* expression does not regulate whisker kinematics in the absence of tactile input. We next quantified whisker dynamics in these same animals during whisking against a stationary pole **(Figure 2M; Video S3)**, a paradigm that approximates the sensing process in the head-fixed pole localization task **(Figure 2D)**. Physical interactions between the whisker and pole during rhythmic whisking induced whisker curvature during individual touch episodes **(Figure2 M-N)**. Each episode of whisker contacting the object (i.e., touch episode) was extracted from the high-speed videos. Contact duration and whisker curvature for each touch episode was calculated for both genotypes. We observed that touch episodes generated smaller changes in whisker curvature in *Syngap1*$^{+/-}$ mice compared to WT controls **(Figure2 N-O)**. Moreover, there was an effect of genotype on touch duration, with *Syngap1*$^{+/-}$ mice exhibiting shorter touch durations than WT controls **(Figure 2P)**. Finally, we categorized touches based on how they influenced touch-induced pumps (TIPs), a specific type of whisker dynamic where the animal purposefully holds the whisker on the pole and engages in a "pumping" behavior once the pole is perceived [60]. We categorized all touches into four TIP categories based on amplitude and acceleration of the whisker while in contact with the pole **(Figure S5; Video S4**). In the category defined by >2 changes in amplitude and acceleration during pole contact, which includes the long-lasting touches with substantial levels of integrated curvature, we found that there were significantly fewer of these touches in *Syngap1* heterozygotes compared to *wildtype* controls **(Figure2Q-R).** Thus, this finding is consistent with both reduced object exploration and reduced tactile sensitivity in *Syngap1*$^{+/-}$ mice.

Syngap1 expression within cortical excitatory neurons promotes perceptual learning, touch sensitivity, and touch-induced changes to whisker motion

Somatosensory systems are distributed throughout the brain and body. Thus, to gain mechanistic insight into the role of *Syngap1* expression on tactile sensing, we sought to identify the regional origins of *Syngap1* expression sufficient to explain tactile phenotypes in this animal model. We hypothesized that *Syngap1* expression within higher-order brain areas may be sufficient to explain its role in both whisker dynamics and tactile learning. This theory was based on literature demonstrating that *Syngap1* is enriched in cortical areas [61,62], combined with separate literature indicating that touch engages top-down MSM loops, which dynamically tune whisker dynamics during sensing by signaling downward to brainstem motor neurons [30,63–65]. To do this, we utilized two established *Syngap1* mouse lines that conditionally regulate the gene's expression in cortical glutamatergic neurons (e.g., *EMX1*+ neurons). One line enables conditional heterozygosity within *EMX1*+ neurons during the mid-embryonic period (*EMX1-Syngap1-OFF*), while the other embryonically re-activates *Syngap1* expression in a heterozygous null background selectively within the EMX1+ population [66,67] (*EMX1-Syngap1-ON*) **(Figure 3A)**. We first assessed whisker kinematics **(Figure 3B)**. No effect of genotype was observed in free air whisking measures in either model **(Figure 3C-E)**, which is consistent with a lack of phenotypes observed in germline (whole body) *Syngap1*$^{+/-}$ null mice (Figure 2h-l). However, during pole presentation **(Figure 3F)**, *EMX1-Syngap1-OFF* heterozygous mice largely phenocopied altered touch-induced whisker kinematics originally observed in germline *Syngap1*$^{+/-}$ mice **(Figure 3G-J; Figure 2N-P)**. Touch episodes were shorter and generated less curvature compared to *Syngap1*$^{+/+}$ littermates. In contrast, *EMX1-Syngap1-"ON"* heterozygous mice did not express touch-regulated whisker motion phenotypes found in the other two models **(Figure 3G-J)**, even though *Syngap1* expression was only re-activated within EMX1+ glutamatergic cortical projection neurons (e.g. thalamic, cerebellar, brain stem areas, as well as the rest of the body remained heterozygous for *Syngap1* expression [60,61]). This result demonstrates that *Syngap1* expression within EMX1+ neurons is necessary and sufficient for regulating touch-induced changes to whisker kinematics during pole exploration.

Syngap1 expression within cortical glutamatergic neurons was also necessary and sufficient for promoting tactile sensitivity. For example, restricting *Syngap1* heterozygosity to cortical excitatory neurons phenocopied germline heterozygosity in the WDIL paradigm – there was a significant reduction in learning over the three-week training period in this task **(Figure 3K; Figure S6A**). In contrast, restricting *Syngap1* heterozygosity to all cells in the body except cortical glutamatergic neurons (i.e., EMX1-*Syngap1-ON*) resulted in no significant differences between genotypes in key measures of learning and trial discrimination **(Figure 3L; Figure S6B).** Moreover, there was no effect of genotype in the pull-back portion of the study **(Figure 3M, Figure S6C),** demonstrating that detection sensitivity was normal in the EMX1+ rescue mice. Lack of phenotypes in the *Syngap1*-ON model was most likely driven by re-expression of *Syngap1* expression in the target neuron population. This interpretation was supported by impaired pull-back sensitivity in non-Cre-expressing *Syngap1*-OFF mice compared to littermate controls **(Figure S6D-E)**. Indeed, these non-Cre expressing mice represent a distinct strain of *Syngap1* heterozygous knockout mice[66]. Thus, this result demonstrates reproducibility of the effect of *Syngap1* expression on tactile sensitivity. *EMX1-Syngap1-ON* mice were also tested in the NOR-T paradigm. Mice with *Syngap1* re-expressed in the EMX1+ population were able to discriminate between the two nearly identical textured objects **(Figure 3N, Figure S6F)**. Importantly, no unexpected germline deletion of LoxP sites[68] was observed in the *EMX1-Syngap1-ON* mice **(Figure S7)**, demonstrating that regulation of *Syngap1* expression was indeed restricted to the expected target population. Together, these data demonstrate that expression of *Syngap1* within cortical glutamatergic neurons is both necessary and sufficient to produce touch-driven whisker control during object exploration, tactile sensitivity, and perceptual learning.

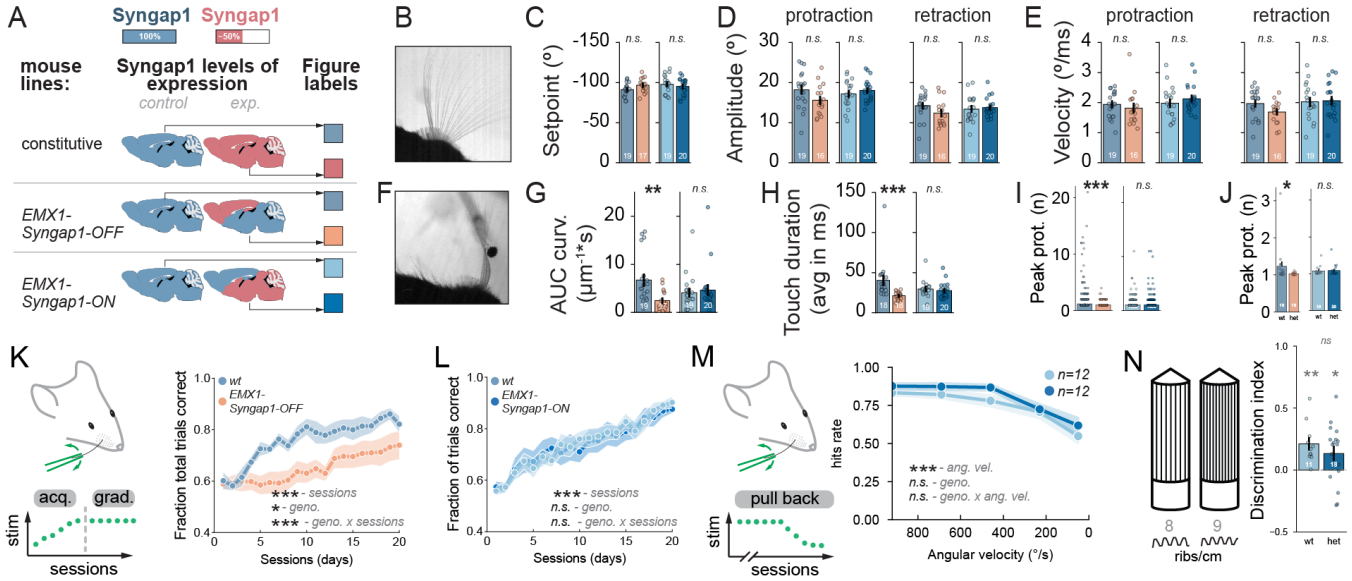

Figure 3. Syngap1 expression within cortical excitatory neurons promotes tactile sensitivity and perceptual learning. A. Mouse line probing the impact of *Syngap1*$^{+/-}$ restricted to cortical excitatory neurons (EMX1-Syngap1-OFF); cortical excitatory neuron rescue of *Syngap1*$^{+/-}$ (EMX1-Syngap1-ON) - all other cells in brain and body remain heterozygous for this gene. B-E Whisker dynamics in free air and during object exploration. Superimposition of 40 frames representing whisking in wt mouse acquired at 500Hz illustrating free whisking of a single whisker (B). Quantification of whisker setpoint (C), amplitude (D) and velocity (E) during the protraction (prot.) and retraction (ret.) whisking phase during a 30 second recording window for the EMX1-Syngap1-OFF and EMX1-Syngap1-ON. F-J Active touch dynamics of a single whisker for the first 30 seconds of pole presentation, superimposition of 40 frames representing active touch (F). Quantification of area under the curve (AUC) for whisker curvature (G), average touch duration (H) and the total number of peak protraction detected for each individual touch event (I) and their respective animal average (J). Color coding of groups is described in (A), n.s.: not significant, *: p<0.05, **: p<0.01, ***: p<0.001). K-N. Modulation of Syngap1 expression in cortical excitatory neuron population in tactile sensitivity assays. Summary schematic of the training phase during passive tactile stimulus (WDIL) and fraction of total trials correct in EMX1-Syngap1-OFF (K) and EMX1-Syngap1-ON (L) mouse lines. M. Hit rate for EMX1-Syngap1-ON animals that reached criteria and underwent the reduced stimulation phase of the WDIL (pull back) .N. Discrimination index during the testing phase of the NOR-T for objects with 10 groves spacing difference in EMX1-Syngap1-ON line. (n.s.: p>0.05, *: p<0.05, **: p<0.01, ***: p<0.001).

Syngap1 regulates circuit connectivity and function within cortical nodes of sensorimotor networks

How could *Syngap1* expression in the cortical excitatory neurons impact tactile sensitivity? The integration of touch signals with motor signals in higher-order sensorimotor loops is thought to enable touch-induced changes to whisker kinematics [30,69], as well as neural computations supporting object localization [70]. Therefore, we hypothesized that *Syngap1* expression in the cortex regulates connectivity of neurons that function within higher-order sensorimotor loops. We targeted connectivity onto Layer 5 (L5) neurons in somatosensory cortex (S1) for two reasons. First, they are known to integrate motor and touch signals [46,71,72]. Second, *Syngap1* regulates the maturation rate of dendritic spine formation and pruning in L5b neurons[73], which are known substrates of circuit assembly and refinement. To test this idea, a cell-type specific rabies virus (RBV) monosynaptic retrograde labeling technique[74] was performed to trace brain-wide synaptic connectivity onto L5 S1 neurons in *Syngap1*$^{+/+}$ and *Syngap1*$^{+/-}$ mice **(Figure 4A-C)**. We achieved regional and neuronal subtype selectivity by crossing *Syngap1*$^{+/-}$ mice to RBP4-Cre mice and then injecting viral vectors directly into S1. Traced neurons within anatomically defined brain areas were registered and quantified[75] **(Figure S8A-D)**. The location of helper and rabies virus injections within L5 S1 was similar across all animals of both genotypes and a similar number of sections from each group was analyzed **(Figure S8E)**. Importantly, no significant difference between genotypes was observed in the number of double labeled L5 S1 starter cells and there was a similar number of inputs (e.g., number of eGFP-only neurons outside L5 S1) relative to the starter cell population **(Figure S8F-J)**. This indicated that the total long-range synaptic connectivity onto L5 S1 neurons was not different between genotypes, which agrees with prior data demonstrating no alteration in spine density of L5 S1 at PND60 in *Syngap1*$^{+/-}$ mice [76].

Based on these initial results, we hypothesized that altered connectivity onto L5 S1 neurons in *Syngap1* mice may be isolated to individual brain areas. To test this idea, we quantified relative connectivity onto L5 S1 neurons for all brain regions and observed a statistical difference only for motor cortex (M1/M2) inputs **(Figure 4D-F)**. Grouping neurons within cortical origins across the antero-posterior axis revealed a genotype effect **(Figure 4G,** Ctx->S1/L5**)**, indicating that afferent connectivity originating from sub-cortical areas was not impacted by *Syngap1* deficiency. The genotype effect of afferent cortical connectivity onto L5 S1 neurons was driven by selective changes in motor cortex areas. Indeed, we observed an increase in eGFP-labeled neurons in M1/M2, but not other cortical areas, in *Syngap1*$^{+/-}$ mice compared to WT controls **(Figure 4D-E)**. Moreover, when neurons originating from motor areas were removed from the "cortex" cluster, this difference was no longer significant **(Figure 4G,** Ctx-M->S1/L5**)**. Furthermore, the increased M1/2 labeling in *Syngap1*$^{+/-}$ mice was driven largely by neurons in deeper layers **(Figure 4G,** M1/L2-3->S1/L5 and M1/L5->S1/L5**)**. Thus, this unbiased screen of synaptic connectivity onto L5 S1 neurons revealed a selective increase in inputs arriving from motor cortex.

To assess the validity of elevated motor-to-somatosensory cortex synaptic connectivity reported by RBV retrograde transsynaptic tracing, we measured the function of this input in *Syngap1* mice. An opto-probe was inserted into motor cortex of *Thy1*-ChR2 mice, which expresses ChR2 selectively within L5 neurons [77]. ChR2+ mice were either WT or Heterozygous for the *Syngap1* null allele. A single-channel electrode was lowered into L5 of S1 to record field potentials **(Figure 4H).** Optogenetic activation within M1/M2 resulted in a biphasic waveform (WF1, WF2; **Figure S9A-C**). TTX injection into the thalamus had an outsized impact on WF2 compared to WF1 **(Figure S9C)**. Given that WF1 occurred within a few milliseconds of the stimulus, these data together indicated that the early peak most likely reflects monosynaptic connections from M1/M2 to S1, while the later peak may reflect a multi-synaptic loop, such as the M1/2 > Thalamus > S1 loop. We observed a significant increase in WF1 in *Syngap1* mutants relative to littermate controls **(Figure 4I-K)**, which was consistent with RBV retrograde tracing data. Moreover, long-range functional hyperconnectivity of M1/2 > S1 in *Syngap1* mice was not generalized, but instead was selective. In contrast to M1/M2 inputs to L5 of S1-BF, whisker deflections, which drive peripherally generated activity that arrives in S1 through thalamic feed-forward excitation, resulted in significantly *smaller* synaptic responses in L5 S1 from *Syngap1*$^{+/-}$ mice compared to WT littermates **(Figure 4L-N)**. Together, these data demonstrate that L5 neurons in S1 of *Syngap1* mice receive a relatively strong input from M1/M2, a con-

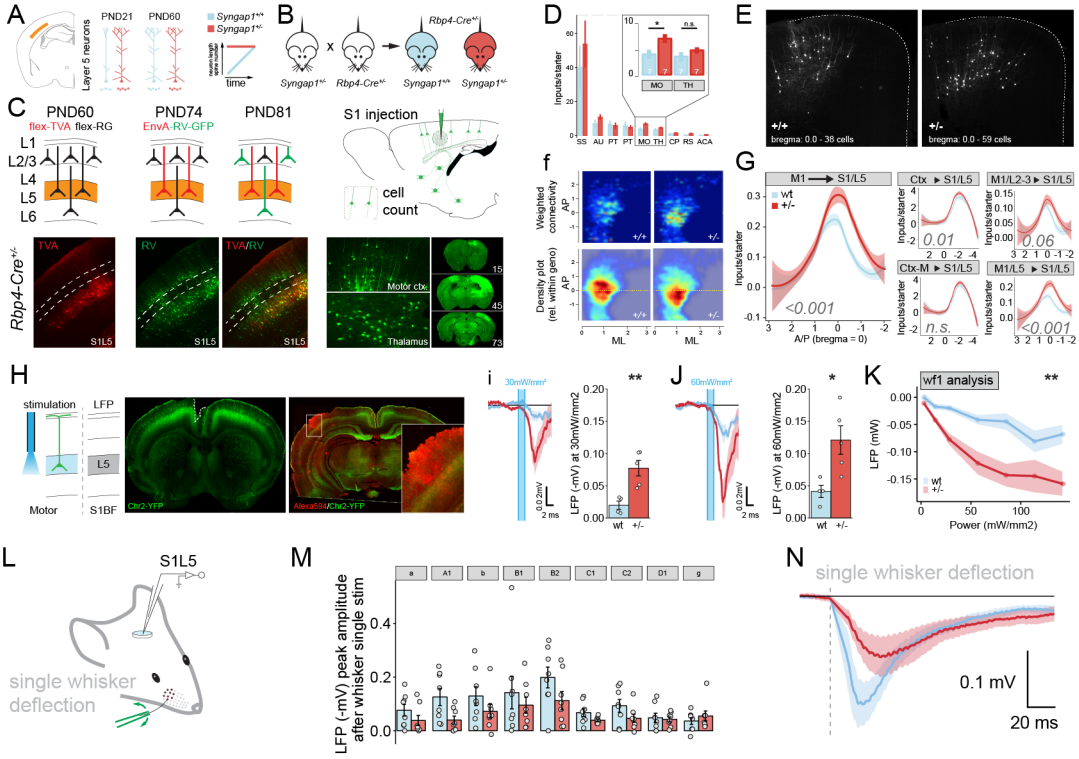

Figure 4. Specific components of the touch circuit within the somato-motor cortex are hyperconnected in *Syngap1*$^{+/-}$ mice. A. Model of accelerated maturation of S1L5 neurons based on prior published work[76] B. Breeding strategy to enable S1L5 input mapping in wildtype and *Syngap1*$^{+/-}$. C. Consecutive steps for cell type specific tracing: AAV transduction of Cre-dependent helper viruses (PND60, flex-TVA and flex-RG), rabies virus transduction (PND74, EnvA-RV-GFP), and rabies virus spread (PND81). Transduction of the helper virus flex-TVA and rabies virus are visualized respectively with the mCherry and GFP (red and green fluorescent signal) D. Quantification of brain area specific inputs of S1L5 neurons normalized to the starter cell population. E. Representative images of monosynaptic inputs from the motor cortex (+/+: WT, $^{+/-}$: *Syngap1*$^{+/-}$). F. Flat map of motor connectivity in antero-posterior (AP) and media-lateral (ML) axes of weighted connectivity averaged across group and their relative within group density plots. G. Quantification of the distribution of inputs to S1L5 normalized to the starter cell population in the antero-posterior axis for inputs from motor cortex, all cortical inputs, all cortical inputs after removing the motor inputs from the quantification, L2/3 motor inputs, L5 motor inputs (blue: WT, n=7; red: *Syngap1*$^{+/-}$, n=7; smoothed conditional means). H. Strategy for optical stimulation of M1L5 neurons and recordings of LFP in S1L5 neurons. I-K. Peak LFP responses in S1L5 after M1L5 stimulation at 30 mW/mm2 (i) and 60mW/mm2 (j) stimulation intensities. K. Peak amplitude of LFP responses from different stimulation intensities in wt (n=5) and *Syngap1*$^{+/-}$ mice (n=4). L. Cartoon representing recording of LFPs during single whisker deflection. M. Individual LFP responses for each whisker stimulated. N. LFP amplitude after single whisker deflection in wt (n=8) and *Syngap1*$^{+/-}$ (n=8) across 9 different whiskers. (n.s.: p>0.05, *: p<0.05, **: p<0.01, ***: p<0.001).

nection that relays whisker motor signals [30,71], but relatively weak afferent thalamocortical connectivity, an important connection that transmits whisker-touch signals into cortex.

L5 neurons in the barrel area of S1 (S1-BF) are known to integrate whisker motor signals with whisker touch signals. The integration of these signals is thought to contribute to both object location and closed-loop changes to whisker kinematics[8,46]. Thus, the circuit connectivity observations in *Syngap1* mice suggest that neurons in this region may have altered activity in response to whisker motion and/or object touch. To directly test this, we measured unit spiking activity in whisker sensorimotor areas, including M1/M2, S1-BF, and whisker thalamus (VPM/POM), in *Syngap1* mice while they whisked in the presence or absence of a pole. Neural activity was recorded simultaneously across these regions in awake head-fixed *Syngap1*$^{+/+}$ and *Syngap1*$^{+/-}$ mice using multi-channel silicon probes **(Figure 5A-D, Figure S10, Figure S11)**. During the two-hour recording period, lighting, auditory white noise, and the presence of a pole were varied to provide animals with a diverse sensory experience. Across the three brain areas, there was no difference in the number of multiunit activity (MUA) clusters extracted from the two genotypes during electrophysiological recordings **(Figure S10B)**. In addition, there was no effect of genotype on the mean peak MUA spike rate in any of the three brain areas when activity was averaged for the entire recording period **(Figure 5E)**. This indicates that the level of ongoing brain activity within the somatomotor network over prolonged time periods is not changed in head-fixed *Syngap1* mice.

Periods of free-air whisking and pole exploration represented only a fraction of the total time during the recording session. Therefore, we hypothesized that genotype-specific changes in neural activity would emerge during specified behavioral epochs defined by whisking with and without the pole present. Discrete free whisking (no pole) and touch (pole present) events were identified from high-speed video recordings **(Video S1).** These events represent two distinct behavioral transitions – from stationary to self-generated whisker movement **(whisking – VideoS2)** and from self-generated whisker motion to object contact inducing curvature **(touch – Video S3)**. We identified whisking and/or touch responsive MUA clusters in each brain area from both genotypes **(Figure 5F)**. In animals from both genotypes, the dynamics of spike rate modulation were distinct in MUA clusters during free whisking compared to touch, and these patterns of activity agreed with past studies using similar recording techniques[78]. For example, free-air whisking units displayed prolonged activity on the order of hundreds of milliseconds, while touch-responsive units displayed activity for much shorter periods of time **(Video S5)**. Distinct unit modulation associated with free whisking and touch is consistent with the unique time scale of the two behaviors. Free whisking bouts were variable, though they usually lasted for hundreds of milliseconds and beyond[79], while individual touches were generally an order of magnitude faster, with 80% of touches lasting less than 50ms **(Figure 2P and 3H; Figure S11C)**. Measuring spike rate modulation during the two distinct behaviors revealed numerous measures with significant genotype effects **(Figure 5G)**. In general, motor signals associated with free whisking were significantly increased in *Syngap1*$^{+/-}$ compared to *Syngap1*$^{+/+}$ mice. Furthermore, the increase in motor activity during free whisking observed in M1 of *Syngap1*$^{+/-}$ mice was also present in S1 and thalamus, with thalamus resembling M1 **(Figure 5G)**, while S1 MUAs demonstrated a less notable increase in activity compared to that observed in M1 and thalamus **(Figure5G)**. Together, these findings demonstrate that *Syngap1* mice have a generalized increase in whisker motor signals within MSM network nodes.

In contrast, touch-related activity was generally decreased across these three regions in *Syngap1* mutants **(Figure 5H)**. Analysis of MUA cluster dynamics during all touch events revealed significantly reduced peak spike rates in *Syngap1*$^{+/-}$ relative to *Syngap1*$^{+/+}$ mice. The general finding of reduced activity across the tactile-motor loop during touch in *Syngap1* mutants is consistent with our findings of reduced curvature of the whisker during individual object touches in animals with reduced expression of *Syngap1* **(Figure 2O; Figure 3G)**. In addition to abnormalities in peak spike rates, there was a clear disparity in the temporal onset of spiking in response to touch in mutants relative to WT littermate controls **(Figure 5H)**. Unit dynamics in *Syngap1*$^{+/-}$ mice appeared to be low-pass filtered compared to WT littermates. In the thalamus, peak touch-dependent modulation was delayed, while duration of touch-related activity was prolonged in *Syngap1*$^{+/-}$ mice compared to WTs **(Figure 5H)**. In M1/M2, a biphasic response was noted in WTs, with a rapid

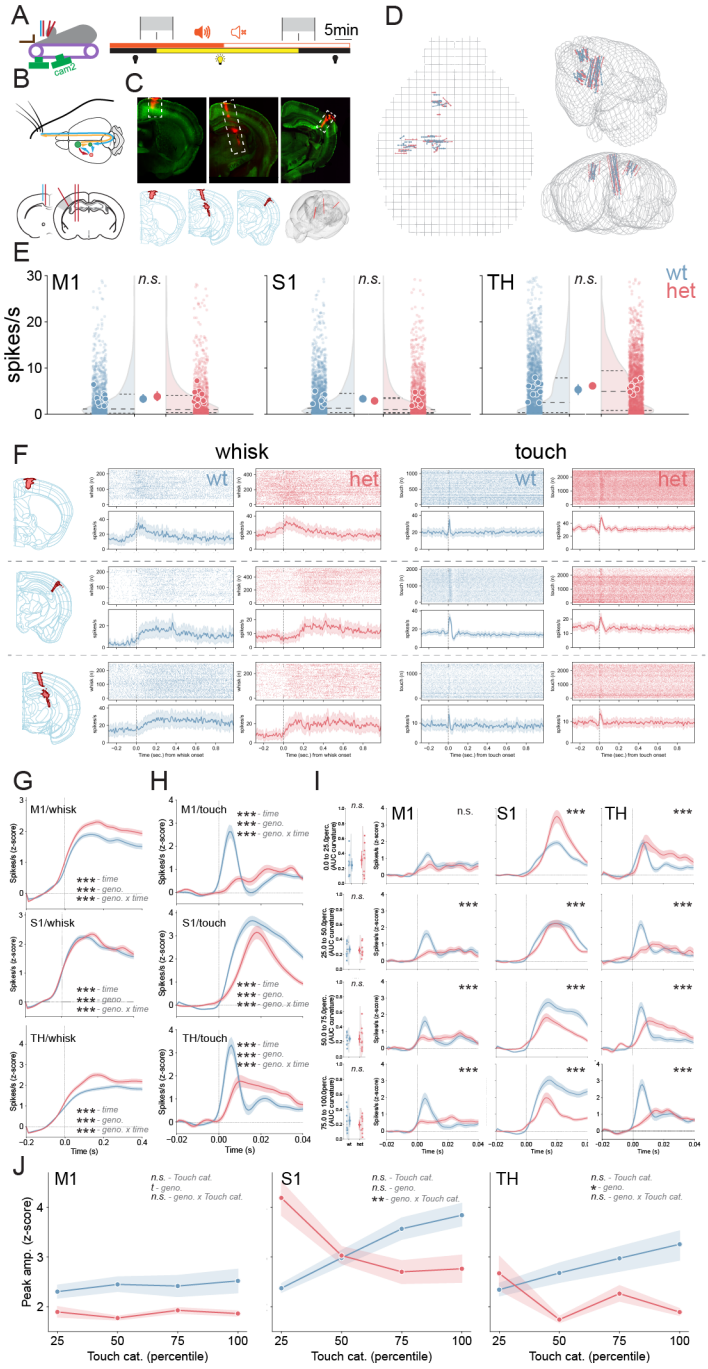

Figure 5. Impaired thalamocortical dynamics during active sensing in *Syngap1*$^{+/-}$ mice. A. Experimental design and timeline during multi-channel silicon probe recordings. B. Schematic of the neural circuitry and probe insertions during the experiment. C. Representative DiI staining of probe implantation in motor cortex, thalamus, and somatosensory cortex (left to right) with reconstructed DiI traces overlayed onto the Allen Brain atlas D. Multi probe track reconstruction in Allen Brain atlas for all wt (blue) and *Syngap1*$^{+/-}$ (red) animals that underwent recordings. E. Average spike rate (spikes/seconds) for extracted cluster including single and multiunit activity for both wt and het in M1, TH and S1. Small dots represent units, larger dots are animal means and largest dot represents group averages. Half violin plots illustrate the unit distributions. F. Raster and PSTH examples of firing for multi-units from M1 (top row), S1 (middle), TH (bottom) in wt and *Syngap1*$^{+/-}$ mice. G-H. Averaged PSTHs for responsive clusters showing spike rates as z-scores during whisking onset (G) and touch (H) for M1, S1 and TH. I-J. Characterization of spike rates (as z-scores) from (H) based on strength of whisker curvature (0-25 %, 25-50 %, 50-75 % and 75-100 % of max whisker curvature) for M1, S1 and TH in wt and *Syngap1*$^{+/-}$ mice and the corresponding peak amplitudes of z-score firing rates for each percentile of whisker touch (J). (n.s.: p>0.05, *: p<0.05, **: p<0.01, ***: p<0.001).

initial peak of activity occurring in response to object touch **(Figure 5H)** and a secondary peak occurring 10-20ms later, which likely reflects recurrent activity arriving from other brain areas. In contrast, the initial peak after touch was absent in *Syngap1*$^{+/-}$ mice, while the delayed responses appeared intact. Importantly, we observed reduced touch-induced spiking within S1-BF integrator units of *Syngap1* mutants, which responded to both whisker motion and pole-touch **(Figure S11E)**.

Reduced touch-related activity in units from *Syngap1*$^{+/-}$ mice could be a consequence of reduced psychomotor properties of the whisker during pole exploration (e.g., reduced average curvature during touch episodes). However, we have reported previously that controlled whisker curvature induced by passive whisker deflections results in reduced calcium-related neuronal activity in S1-BF from *Syngap1* mutants[23]. Thus, it is also possible that *Syngap1*$^{+/-}$ somatomotor networks may encode fewer spikes per unit of curvature. To resolve these two possibilities, we clustered all touch events into four categories based on integrated total whisker curvature in response to pole contact (e.g., “small”, “medium”, “large”, and “extra-large” levels of curvature). When categorized this way, there was no difference in curvature between the genotypes within any of the four touch categories **(Figure 5I)**. As a result, touch-responsive units could now be compared between genotypes in the context of similar average levels of curvature. When unit activity was reanalyzed across the four touch categories in each genotype, surprising results were obtained. In WT mice, the expected positive correlation between curvature category and average peak spike rate in all three brain areas was present **(Figure 5J)**. However, in *Syngap1*$^{+/-}$ mice, this relationship was essentially inverted. For example, there was a clear negative correlation between the magnitude of average curvature and average unit spike rate in both S1-BF and thalamus. Indeed, in S1-BF, touches that generated the greatest whisker curvature had the least amount of associated unit activity **(Figure 5I-J)**. Taken together, touch elicits weak and temporally altered spiking activity in units from all three somatomotor areas in *Syngap1* mutants, while units that responded to whisking exhibited enhanced activity in these same areas.

Discussion

The molecular and cellular mechanisms that link SMI in higher brain regions to cognitive constructs that support adaptive behavior are poorly understood. The motivation behind this study was to investigate the relationships between the neurobehavioral correlates of SMI that promote cognitive functions and genetic risk associated with intellectual impairments. In this study, we investigated how the major intellectual disability and autism risk gene, *Syngap1,* regulates sensorimotor processes in the cortex that support higher cognitive functions. To understand how *Syngap1* contributes to SMI, we independently investigated how it contributes to sensory and motor processing underlying tactile sensing with whiskers. We also investigated the role of this gene directly in SMI through combined behavioral and electrophysiological observations during active whisker touch. Together, these data converged on a model where *Syngap1* promotes tactile perception and associated behavioral reactivity by assembling circuits that initially represent touch in the cortex. These circuits also integrate touch signals with whisker motor signals to promote an understanding of object features, such as location and texture.

Initially, we established that *Syngap1* loss-of-function leads to behavioral *hypo*-sensitivity when sensing with whiskers, which is expressed across tactile domains, including detection sensitivity, texture discrimination, and object localization **(Figure 6A)**. These mouse studies are consistent with reports of tactile hyposensitivity and very high pain thresholds in *SYNGAP1-DEE* patients, including impaired behavioral reactivity in response to external stimuli applied to the body [23,80]. Importantly, similar to the mouse model, this human patient population is defined by heterozygous loss-of-function variants within the *SYNGAP1* gene. Second, we found that *Syngap1* expression in cortical excitatory neurons is both necessary and sufficient for setting tactile detection thresholds that drive perception and associated adaptive behaviors **(Figure 3)**. For example, well-trained *Syngap1* mutant mice made more perceptual errors relative to WT littermates in a subset of trials designed to measure tactile sensitivity. This suggested that poor learning in the tactile domain displayed by *Syngap1* mice may be explained, in part, through reduced whisker sensitivity. This phe-

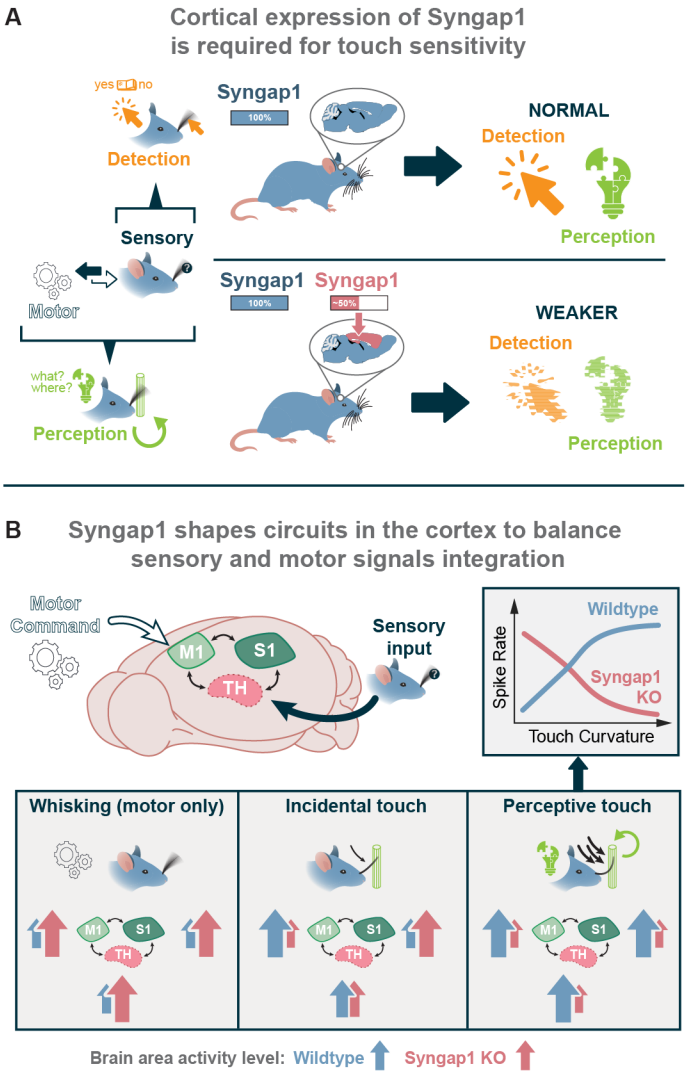

Figure 6. Model for how Syngap1 expression shapes tactile sensitivity and perceptual behaviors through regulation of cortical SMI circuitry. A. When a *Syngap1*$^{+/-}$ animals explore objects with whiskers, touch information is poorly encoded in cortex, which prevents attentional processes from engaging a state-switch, which leads to reduced exploration times. Reduced exploration time will overtly decrease the opportunity for whiskers to code tactile signals required to compute object features. This impacts the strength of a tactile percept, which will impair perceptual learning and associated adaptive behaviors. B. In these mice, the touch signals that arrive in the cortex during the shortened object exploration are weakly encoded. In L5 somatosensory cortex, these weak touch signals are integrated with overly strong whisker motion (motor) signals, a SNR deficit that will degrade the ability of circuits to compute touch and texture features. Indeed, whisker motion and whisker touch generate two distinct streams of information at the level of the whisker follicle. The motor stream carries real-time whisker location information, while the touch stream contains a code for when touch occurred and how strong it was (through whisker curvature). These streams of information are integrated in barrel cortex L5 neurons, which enables an understanding of where the object rests relative to the head. This model can explain how Syngap1 mice learn so poorly within the tactile domain. It is important to note that we also demonstrate that perceptual behaviors are disrupted when biased toward whisker touch, but perception is intact for similar tasks when multisensory processes are available to the Syngap1 animal.

notype was linked to its expression in cortical excitatory neurons because perceptual errors associated with whisker stimulus detection sensitivity were phenocopied in a mouse model with reduced *Syngap1* expression restricted to this population. Moreover, when *Syngap1* expression was re-expressed only in this population, perceptual errors linked to whisker sensitivity were no longer present. A similar rescue of texture discrimination was observed in the *Syngap1* cortex-specific re-expression model. These findings, when integrated with past studies of other NDD risk factors, highlight the principle that individual genes can either promote or suppress neural mechanisms that dictate tactile sensitivity. Several NDD genes, such as *Shank3*, *Mecp2, and Fmr1* have been shown to regulate tactile sensitivity [19,81]. However, for these risk factors, gene loss-of-function was linked to tactile *hyper*-sensitivity rather than *hypo*-sensitivity, which was explained by either cell-autonomous expression within the peripheral nervous system or in the CNS [19,22,82–84]. Moreover, these studies focused on behavioral reactivity, and therefore did not link risk gene expression to neural correlates of cognitive constructs. The uniqueness of *Syngap1* with respect to tactile sensitivity in the context of these mouse studies is important because tactile hyposensitivity is also relatively common in NDD populations, including ASD [26,82,85–88]. Thus, the *Syngap1*$^{+/-}$ mouse line is emerging as a genetic model potentially useful for elucidating the neural correlates linking NDD-associated sensory hyposensitivity to cognitive functions underlying adaptive behavior. In line with this, subsequent experiments in this study were aimed at understanding the potential neurobehavioral and neurophysiological correlates linking tactile hyposensitivity driven by *Syngap1* loss-of-function to impaired cognitive constructs.

Subsequent experiments led to a framework where *Syngap1* function within cortical glutamatergic neurons promotes tactile sensitivity through coding of touch signals in cortical somatomotor networks **(Figure 6B)**. Several lines of evidence support this framework. *First*, impaired responses to passive whisker stimuli within cortical somatomotor areas of *Syngap1* mice is consistent with weak perceptual learning and reduced tactile sensitivity in the passive WDIL task. Our past studies have demonstrated that passive whisker deflections, the stimuli in WDIL, are weakly registered in barrel cortex of *Syngap1* mice, and this neurophysiological observation was dependent on *Syngap1* expression in the EMX1+ population [23]. In that prior study, we noted that increased stimulus intensity of the whisker input in *Syngap1* mice caused larger deficits in barrel cortex activity compared to WT littermates. Whereas increasing stimulus intensity in WT mice led to larger cortical activation, this input/output relationship was impaired in *Syngap1* mice. Similarly, in this current study, we found that increasing the intensity of the stimulus during WDIL training induced more robust learning in WT mice. However, in *Syngap1* mutant mice, this was not the case. Increasing the stimulus intensity in these animals did not generate proportionally better learning as it did in WT, which led to qualitative differences in learning between genotypes **(Figure 1)**. Thus, in these mice, there is a clear correlation between weak somatosensory cortex responses to passive whisker deflections and weak learning related to this same stimulus. Importantly, both behavioral reactivity to (Figure 3), and cortical representations of [23], the passive whisker stimulus are dependent upon *Syngap1* expression in cortical glutamatergic neurons.

Second, we observed abnormal touch-induced whisker exploratory behavior in *Syngap1* mice **(Figure 2)**, including a reduction in the frequency and duration of touch-induced pumps (TIPs). This phenotype is also consistent with poor touch coding within cortical sensorimotor networks. Touch coding within higher-order motor-sensory-motor (MSM) loops is believed to generate touch-induced changes to whisker kinematics observed during active tactile sensing [30,60,64,79]. Tactile signals representing initial object touch are believed to engage higher-order circuits that support constructs of cognition, such as attention [60,79,89]. This leads to a shift in whisker sensing, with motion directed toward focused object exploration by the animal, which includes prolonged and purposeful object contacts that generate high levels of whisker curvature (e.g., TIPs). Thus, weak higher-order registration of initial object contacts in cortical networks is consistent with disrupted touch-induced whisker kinematics during object exploration. According to the existing model, touch signals in higher-order sensorimotor loops trigger prolonged object interactions by altering the function of whisker motor circuits in the brainstem [30,64,65]. In support of this theory, we observed normal whisker kinematics in *Syngap1* mice during free-air whisking. Altered whisker kinematics were observed only when animals were presented with a stationary pole. This result would infer that the *Syngap1* expression in higher brain areas may be required to sustain object exploration by linking touch signals to attentional processes. This theory was additionally supported by the finding that *Syngap1* expression within the cortical excitatory neuron population is both necessary and sufficient for touch-induced changes to whisker kinematics **(Figure3)**. Therefore, *Syngap1* expression likely regulates neurobiological processes within this restricted neuronal population to promote integration of touch sig-

nals into attentional circuits that modulate whisker motor neurons in the brainstem. One possible cellular mechanism may involve the regulation of connectivity and/or function of cortical excitatory neurons that both code for touch and signal to brainstem neurons that drive whisker motion. This possibility was supported through our electrophysiological observations of reduced touch responses in units within higher-order somatomotor loops from *Syngap1* mutants **(Figure 5)**. Future studies will be necessary to determine the extent to which *Syngap1* expression regulates touch-responsive neurons in the cortex that project to brainstem whisker motor circuits.

Third, we observed weak touch responses during pole exploration across higher-order somatomotor areas in *Syngap1* mice, including somatosensory and motor cortex, as well as whisker areas in thalamus **(Figure 5)**. In these mutant animals, weak touch responses were present in the context of an increase in temporally-overlapping whisker motor signals. This sensorimotor imbalance reflected a real change in the signal-to-noise ratio of neurons that integrate touch with whisker motion. Importantly, we observed weak whisker touch responses in neurons from the barrel region of somatosensory cortex that also respond to whisker motion. This is a direct electrophysiological demonstration of altered SMI within the cortex of *Syngap1* animals. Reduced signal-to-noise for touch/motor integration is consistent with impaired object localization. Object localization is thought to be computed, in part, through convergent whisker touch and motor signals that are integrated within cortical sensory and motor areas [30]. Electrophysiological correlates of reduced touch coding, as well as correlates of enhanced motor signals, were supported by circuit tracing and subsequent functional circuit validation studies in *Syngap1* mice. *Syngap1* mice had hyper-functional inputs from motor cortex that project to Layer 5 somatosensory cortex (Figure 4). These mice also possess a weak subcortical input that transmits touch signals into L5 somatosensory cortex.

It is unclear how reduced *Syngap1* expression in mice can cause impaired cortical touch representations, while also causing increased whisker motor representations. Understanding this dichotomy will provide insight into the neural correlates of impaired sensorimotor processing in NDDs. *Syngap1* expression may exert unique cell-autonomous functions within neuronal subtypes that comprise the EMX1+ population. Unique, cell-autonomous functional control over expression of neuronal features that directly assemble and refine circuits could lead to unpredictable circuit-specific impairments, not unlike what was observed in this current study. This hypothesis is supported by evidence in past studies demonstrating that *Syngap1* potently regulates cellular substrates of circuit assembly and refinement, such as dendritic morphogenesis, synaptic maturation, and cell/circuit-level forms of neural plasticity [90]. Intriguingly, *Syngap1* regulates circuit-building substrates in a cell- and region-specific manner, sometimes in opposite directions. For example, it can both promote[76] and constrain[23] dendritic morphogenesis within distinct EMX1+ neuronal subtypes during developmental critical periods. Pertinent to this current study, the developmental maturation of L5b tufted neurons in somatosensory cortex is greatly accelerated in *Syngap1* mutant mice. These *Syngap1*-deficient neurons reach adult-levels of maturation weeks before similar neurons in WT littermates [76]. This accelerated maturation spans major morphogenic developmental milestones, including accelerated dendritic differentiation, early acquisition of dendritic spines, and subsequent precocious spine pruning. In contrast, in this same model, and within the same brain area (somatosensory cortex), the development of L2/3/4 upper-lamina neurons feature arrested development [23]. Altered maturation of neurons in cortex is not restricted to somatosensory cortex [76]. De-synchronization of postmitotic dendritic and synaptic maturation across distinct neuronal subtypes and regions is consistent with impaired somatosensory network function observed in this study. However, a major question remains: are these bespoke changes to neuronal subtypes cell autonomous, or do they reflect complex forms of systems-level homeostatic compensation? Indeed, accelerated maturation of L5 somatosensory cortex neurons could be a non-cell-autonomous compensatory process driven by arrested development and hypofunction of upper lamina excitatory neurons in the same cortical area. This question can be addressed though future studies that leverage intersectional genetic perturbation approaches capable of targeting gene expression specifically within a defined neuronal subtype (e.g., L5 IT or PT neurons) within a restricted brain area (e.g., somatosensory or motor cortex).

Methods

See Supplemental Information.

Acknowledgements

This study was supported by funding provided by NIMH (MH096847) and NINDS (NS110307) to G.R./C.A.M and G.R. (w/D.O. as CO-I), respectively. We thank Gogce C. Crynen, PhD, Director of the UF Scripps Biostatistics Core, for consultation on appropriate application of statistical models to complex data sets.

Author Contributions

T.V and S.D.M. performed experiments, designed experiments, analyzed data, co-wrote the manuscript, and edited the manuscript. T.C. performed experiments, designed experiments, analyzed data, and edited the manuscript. D.F. analyzed and interpreted data. D.B. analyzed and interpreted data. C.R. performed experiments, designed experiments, and generated reagents. R.G. designed experiments and generated data. K.M. provided key reagents and interpreted data. C.A.M secured funding, designed experiments, interpreted data, and edited the manuscript. D.O. designed experiments, interpreted data, edited the manuscript. G.R. conceived the study, secured funding, designed experiments, interpreted data, co-wrote the manuscript, and edited the manuscript.

Declaration of Interests

The authors declare no competing interests.

References

1. Siegel, M., Buschman, T. J. & Miller, E. K. Cortical information flow during flexible sensorimotor decisions. Science 348, 1352–1355 (2015).
2. Pape, A.-A., Noury, N. & Siegel, M. Motor actions influence subsequent sensorimotor decisions. Sci Rep 7, 15913 (2017).
3. Huber, D. et al. Multiple dynamic representations in the motor cortex during sensorimotor learning. Nature 484, 473–478 (2012).
4. J.T. Wixted, J.T. Serences (Eds.), The Stevens Handbook of Experimental Psychology and Cognitive Neuroscience: Sensation, Perception, and Attention, Vol. II (2018). The neural basis of haptic perception. (2018).
5. Karadimas, S. K. et al. Sensory cortical control of movement. Nat Neurosci 23, 75–84 (2020).
6. Yamawaki, N., Raineri Tapies, M. G., Stults, A., Smith, G. A. & Shepherd, G. M. Circuit organization of the excitatory sensorimotor loop through hand/forelimb S1 and M1. eLife 10, e66836 (2021).
7. Yu, C., Derdikman, D., Haidarliu, S. & Ahissar, E. Parallel Thalamic Pathways for Whisking and Touch Signals in the Rat. PLOS Biology 4, e124 (2006).
8. Diamond, M. E., von Heimendahl, M., Knutsen, P. M., Kleinfeld, D. & Ahissar, E. 'Where' and 'what' in the whisker sensorimotor system. Nat Rev Neurosci 9, 601–612 (2008).
9. O'Connor, D. H., Krubitzer, L. & Bensmaia, S. Of mice and monkeys: Somatosensory processing in two prominent animal models. Prog Neurobiol 102008 (2021) doi:10.1016/j.pneurobio.2021.102008.
10. Kleinfeld, D. & Deschênes, M. Neuronal Basis for Object Location in the Vibrissa Scanning Sensorimotor System. Neuron 72, 455–468 (2011).
11. Halley, A. C., Baldwin, M. K. L., Cooke, D. F., Englund, M. & Krubitzer, L. Distributed Motor Control of Limb Movements in Rat Motor and Somatosensory Cortex: The Sensorimotor Amalgam Revisited. Cerebral Cortex 30, 6296–6312 (2020).
12. Shepherd, G. M. G. & Yamawaki, N. Untangling the cortico-thalamo-cortical loop: cellular pieces of a knotty circuit puzzle. Nat Rev Neurosci 22, 389–406 (2021).
13. Dalton, K. M. et al. Gaze fixation and the neural circuitry of face processing in autism. Nat Neurosci 8, 519–526 (2005).
14. Gowen, E. & Hamilton, A. Motor abilities in autism: a review using a computational context. J Autism Dev Disord 43, 323–344 (2013).
15. Fournier, K. A., Hass, C. J., Naik, S. K., Lodha, N. & Cauraugh, J. H. Motor coordination in autism spectrum disorders: a synthesis and meta-analysis. J Autism Dev Disord 40, 1227–1240 (2010).
16. Abbruzzese, G. & Berardelli, A. Sensorimotor integration in movement disorders. Mov Disord 18, 231–240 (2003).
17. Tamilselvam, Y. K., Jog, M. & Patel, R. V. Robot-assisted investigation of sensorimotor control in Parkinson's disease. Sci Rep 13, 4751 (2023).
18. Neeper, R. & Greenwood, R. S. On the Psychiatric Importance of Neurological Soft Signs. in Advances in Clinical Child Psychology (eds. Lahey, B. B. & Kazdin, A. E.) 217–258 (Springer US, 1987). doi:10.1007/978-1-4613-9826-4_6.
19. Orefice, L. L. Outside-in: Rethinking the etiology of autism spectrum disorders. Science 366, 45–46 (2019).
20. He, C. X. et al. Tactile Defensiveness and Impaired Adaptation of Neuronal Activity in the Fmr1 Knock-Out Mouse Model of Autism. J Neurosci 37, 6475–6487 (2017).
21. Burgdorf, J. S. et al. An IGFBP2-derived peptide promotes neuroplasticity and rescues deficits in a mouse model of Phelan-McDermid syndrome. Mol Psychiatry 28, 1101–1111 (2023).
22. Orefice, L. L. et al. Targeting Peripheral Somatosensory Neurons to Improve Tactile-Related Phenotypes in ASD Models. Cell 178, 867-886.e24 (2019).
23. Michaelson, S. D. et al. SYNGAP1 heterozygosity disrupts sensory processing by reducing touch-related activity within somatosensory cortex circuits. Nat Neurosci 21, 1–13 (2018).
24. Klintwall, L. et al. Sensory abnormalities in autism: A brief report. Research in Developmental Disabilities 32, 795–800 (2011).
25. Marco, E. J., Hinkley, L. B. N., Hill, S. S. & Nagarajan, S. S. Sensory Processing in Autism: A Review of Neurophysiologic Findings. Pediatr Res 69, 48–54 (2011).
26. Robertson, C. E. & Baron-Cohen, S. Sensory perception in autism. Nat Rev Neurosci 18, 671–684 (2017).
27. Greven, C. U. et al. Sensory Processing Sensitivity in the context of Environmental Sensitivity: A critical review and development of research agenda. Neuroscience & Biobehavioral Reviews 98, 287–305 (2019).
28. Stevenson, R. A. et al. Multisensory Temporal Integration in Autism Spectrum Disorders. J. Neurosci. 34, 691–697 (2014).
29. Satterstrom, F. K. et al. Large-Scale Exome Sequencing Study Implicates Both Developmental and Functional Changes in the Neurobiology of Autism. Cell 180, 568-584.e23 (2020).
30. Staiger, J. F. & Petersen, C. C. H. Neuronal Circuits in Barrel Cortex for Whisker Sensory Perception. Physiological Reviews 101, 353–415 (2021).
31. Koshiyama, D. et al. Hierarchical Pathways from Sensory Processing to Cognitive, Clinical, and Functional Impairments in Schizophrenia. Schizophr Bull 47, 373–385 (2021).
32. Goel, A. et al. Impaired perceptual learning in a mouse model of Fragile X syndrome is mediated by parvalbumin neuron dysfunction and is reversible. Nat Neurosci 21, 1404–1411 (2018).
33. Pastor-Cerezuela, G., Fernández-Andrés, M.-I., Sanz-Cervera, P. & Marín-Suelves, D. The impact of sensory processing on executive and cognitive functions in children with autism spectrum disorder in the school context. Research in Developmental Disabilities 96, 103540 (2020).
34. Lyons-Warren, A. M., McCormack, M. C. & Holder, J. L. Sensory Processing Phenotypes in Phelan-McDermid Syndrome and SYNGAP1-Related Intellectual Disability. Brain Sci 12, 137 (2022).
35. Holder, J. L., Hamdan, F. F. & Michaud, J. L. SYNGAP1-Related Intellectual Disability. in GeneReviews® (eds. Adam, M. P. et al.) (University of Washington, Seattle, 1993).
36. Hamdan, F. F. et al. Mutations in SYNGAP1 in Autosomal Nonsyndromic Mental Retardation. N Engl J Med 360, 599–605 (2009).
37. Vlaskamp, D. R. M. et al. SYNGAP1 encephalopathy. Neurology 92, e96–e107 (2019).
38. Parker, M. J. et al. De novo, heterozygous, loss□of□function mutations in SYNGAP1 cause a syndromic form of intellectual disability. Am J Med Genet A 167, 2231–2237 (2015).
39. Mignot, C. et al. Genetic and neurodevelopmental spectrum of SYNGAP1-associated intellectual disability and epilepsy. Journal of Medical Genetics 53, 511–522 (2016).
40. Carreño-Muñoz, M. I. et al. Sensory processing dysregulations as reliable translational biomarkers in SYNGAP1 haploinsufficiency. Brain 145, 754–769 (2022).
41. Nakajima, R. et al. Comprehensive behavioral analysis of heterozygous Syngap1 knockout mice. Neuropsychopharmacol Rep 39, 223–237 (2019).
42. Verschure, P. F. M. J., Pennartz, C. M. A. & Pezzulo, G. The why, what, where, when and how of goal-directed choice: neuronal and computational principles. Philos Trans R Soc Lond B Biol Sci 369, 20130483 (2014).
43. Zagha, E. et al. The Importance of Accounting for Movement When Relating Neuronal Activity to Sensory and Cognitive Processes. J. Neurosci. 42, 1375–1382 (2022).
44. Kleinfeld, D., Ahissar, E. & Diamond, M. E. Active sensation: insights from the rodent vibrissa sensorimotor system. Curr Opin Neurobiol 16, 435–444 (2006).
45. Feldmeyer, D. et al. Barrel cortex function. Progress in Neurobiology 103, 3–27 (2013).
46. Petersen, C. C. H. Sensorimotor processing in the rodent barrel cortex. Nat Rev Neurosci 20, 533–546 (2019).
47. Esmaeili, V. et al. Cortical circuits for transforming whisker sensation into goal-directed licking. Current Opinion in Neurobiology 65, 38–48 (2020).
48. Petersen, C. C. H., Knott, G. W., Holtmaat, A. & Schürmann, F. Toward Biophysical Mechanisms of Neocortical Computation after 50 Years of Barrel Cortex Research. Function 2, zqaa046 (2021).
49. Sherman, D., Oram, T., Harel, D. & Ahissar, E. Attention Robustly Gates a Closed-Loop Touch Reflex. Curr Biol 27, 1836-1843.e7 (2017).
50. O'Connor, D. H., Krubitzer, L. & Bensmaia, S. Of mice and monkeys: Somatosensory processing in two prominent animal models. Prog Neurobiol 102008 (2021) doi:10.1016/j.pneurobio.2021.102008.
51. Llamosas, N. et al. Syngap1 regulates experience-dependent cortical ensemble plasticity by promoting in vivo excitatory synapse strengthening. Proc Natl Acad Sci U S A 118, e2100579118 (2021).
52. Zhao, M. & Kwon, S. E. Interneuron-targeted disruption of SYNGAP1 alters sensory representations in neocortex and impairs sensory learning. 2022.09.27.509690 Preprint at https://doi.org/10.1101/2022.09.27.509690 (2022).
53. Yang, H., Kwon, S. E., Severson, K. S. & O'Connor, D. H. Origins of choice-related activity in mouse somatosensory cortex. Nat Neurosci 19, 127–134 (2016).
54. Gibson, J. J. Observations on active touch. Psychological Review 69, 477–491 (1962).
55. Szwed, M., Bagdasarian, K. & Ahissar, E. Encoding of Vibrissal Active Touch. Neuron 40, 621–630 (2003).

56. Pluta, S. R., Lyall, E. H., Telian, G. I., Ryapolova-Webb, E. & Adesnik, H. Surround Integration Organizes a Spatial Map during Active Sensation. Neuron 94, 1220-1233.e5 (2017).
57. Xu, N. et al. Nonlinear dendritic integration of sensory and motor input during an active sensing task. Nature 492, 247–251 (2012).
58. O'Connor, D. H. et al. Vibrissa-Based Object Localization in Head-Fixed Mice. J. Neurosci. 30, 1947–1967 (2010).
59. Mathis, A. et al. DeepLabCut: markerless pose estimation of user-defined body parts with deep learning. Nat Neurosci 21, 1281–1289 (2018).
60. Deutsch, D., Pietr, M., Knutsen, P. M., Ahissar, E. & Schneidman, E. Fast Feedback in Active Sensing: Touch-Induced Changes to Whisker-Object Interaction. PLOS ONE 7, e44272 (2012).
61. Kim, J. H., Liao, D., Lau, L. F. & Huganir, R. L. SynGAP: a synaptic RasGAP that associates with the PSD-95/SAP90 protein family. Neuron 20, 683–691 (1998).
62. Porter, K., Komiyama, N. H., Vitalis, T., Kind, P. C. & Grant, S. G. N. Differential expression of two NMDA receptor interacting proteins, PSD-95 and SynGAP during mouse development. Eur J Neurosci 21, 351–362 (2005).
63. Ahissar, E. & Assa, E. Perception as a closed-loop convergence process. eLife 5, e12830 (2016).
64. Petersen, C. C. H. The Functional Organization of the Barrel Cortex. Neuron 56, 339–355 (2007).
65. Nguyen, Q.-T. & Kleinfeld, D. Positive feedback in a brainstem tactile sensorimotor loop. Neuron 45, 447–457 (2005).
66. Clement, J. P. et al. Pathogenic SYNGAP1 mutations impair cognitive development by disrupting maturation of dendritic spine synapses. Cell 151, 709–723 (2012).
67. Gorski, J. A. et al. Cortical Excitatory Neurons and Glia, But Not GABAergic Neurons, Are Produced in the Emx1-Expressing Lineage. J. Neurosci. 22, 6309–6314 (2002).
68. Luo, L. et al. Optimizing Nervous System-Specific Gene Targeting with Cre Driver Lines: Prevalence of Germline Recombination and Influencing Factors. Neuron 106, 37-65.e5 (2020).
69. Wallach, A., Deutsch, D., Oram, T. B. & Ahissar, E. Predictive whisker kinematics reveal context-dependent sensorimotor strategies. PLoS Biol 18, e3000571 (2020).
70. Cheung, J., Maire, P., Kim, J., Sy, J. & Hires, S. A. The Sensorimotor Basis of Whisker-Guided Anteroposterior Object Localization in Head-Fixed Mice. Curr Biol 29, 3029-3040.e4 (2019).
71. Manita, S. et al. A Top-Down Cortical Circuit for Accurate Sensory Perception. Neuron 86, 1304–1316 (2015).
72. Feldmeyer, D. Excitatory neuronal connectivity in the barrel cortex. Front Neuroanat 6, 24 (2012).
73. Aceti, M. et al. Syngap1 haploinsufficiency damages a postnatal critical period of pyramidal cell structural maturation linked to cortical circuit assembly. Biol Psychiatry 77, 805–815 (2015).
74. Miyamichi, K. et al. Dissecting local circuits: parvalbumin interneurons underlie broad feedback control of olfactory bulb output. Neuron 80, 1232–1245 (2013).
75. Fürth, D. et al. An interactive framework for whole-brain maps at cellular resolution. Nat Neurosci 21, 139–149 (2018).
76. Aceti, M. et al. Syngap1 Haploinsufficiency Damages a Postnatal Critical Period of Pyramidal Cell Structural Maturation Linked to Cortical Circuit Assembly. Biological Psychiatry 77, 805–815 (2015).
77. Arenkiel, B. R. et al. In vivo light-induced activation of neural circuitry in transgenic mice expressing channelrhodopsin-2. Neuron 54, 205–218 (2007).
78. Yu, J., Hu, H., Agmon, A. & Svoboda, K. Recruitment of GABAergic Interneurons in the Barrel Cortex during Active Tactile Behavior. Neuron 104, 412-427.e4 (2019).
79. Mitchinson, B. et al. Active vibrissal sensing in rodents and marsupials. Philosophical Transactions of the Royal Society B: Biological Sciences 366, 3037–3048 (2011).
80. Barco, T. L. et al. SYNGAP1-related developmental and epileptic encephalopathy: The impact on daily life. Epilepsy Behav 127, (2022).
81. Schaffler, M. D., Middleton, L. J. & Abdus-Saboor, I. Mechanisms of Tactile Sensory Phenotypes in Autism: Current Understanding and Future Directions for Research. Curr Psychiatry Rep 21, 134 (2019).
82. Orefice, L. L. Peripheral Somatosensory Neuron Dysfunction: Emerging Roles in Autism Spectrum Disorders. Neuroscience 445, 120–129 (2020).
83. Chen, Q. et al. Dysfunction of cortical GABAergic neurons leads to sensory hyper-reactivity in a Shank3 mouse model of ASD. Nat Neurosci 23, 520–532 (2020).
84. Orefice, L. L. et al. Peripheral Mechanosensory Neuron Dysfunction Underlies Tactile and Behavioral Deficits in Mouse Models of ASDs. Cell 166, 299–313 (2016).
85. Cascio, C. J. Somatosensory processing in neurodevelopmental disorders. J Neurodevelop Disord 2, 62–69 (2010).
86. He, J. L. et al. Disorder-specific alterations of tactile sensitivity in neurodevelopmental disorders. Commun Biol 4, 1–15 (2021).
87. Jung, J. et al. Associations between physiological and neural measures of sensory reactivity in youth with autism. J Child Psychol Psychiatry 62, 1183–1194 (2021).
88. SFARI | Approaches for measuring sensory function in ASD/NDD. SFARI https://www.sfari.org/2023/04/25/approaches-for-measuring-sensory-function-in-asd-ndd/ (2023).
89. Cohen, J. D., Hirata, A. & Castro-Alamancos, M. A. Vibrissa sensation in superior colliculus: wide-field sensitivity and state-dependent cortical feedback. J Neurosci 28, 11205–11220 (2008).
90. Kilinc, M. et al. Species-conserved SYNGAP1 phenotypes associated with neurodevelopmental disorders. Molecular and Cellular Neuroscience 91, 140–150 (2018).
91. Kim, J. H., Lee, H.-K., Takamiya, K. & Huganir, R. L. The role of synaptic GTPase-activating protein in neuronal development and synaptic plasticity. J Neurosci 23, 1119–1124 (2003).
92. Slotnick, B. A simple 2-transistor touch or lick detector circuit. J Exp Anal Behav 91, 253–255 (2009).
93. Tuscher, J. J., Fortress, A. M., Kim, J. & Frick, K. M. Regulation of object recognition and object placement by ovarian sex steroid hormones. Behav Brain Res 285, 140–157 (2015).
94. Clack, N. G. et al. Automated Tracking of Whiskers in Videos of Head Fixed Rodents. PLoS Comput Biol 8, e1002591 (2012).
95. Pammer, L. et al. The mechanical variables underlying object localization along the axis of the whisker. J Neurosci 33, 6726–6741 (2013).
96. Severson, K. S. et al. Active Touch and Self-Motion Encoding by Merkel Cell-Associated Afferents. Neuron 94, 666-676.e9 (2017).
97. Shamash, P., Carandini, M., Harris, K. & Steinmetz, N. A tool for analyzing electrode tracks from slice histology. 447995 Preprint at https://doi.org/10.1101/447995 (2018).
98. Harrison, T. C., Sigler, A. & Murphy, T. H. Simple and cost-effective hardware and software for functional brain mapping using intrinsic optical signal imaging. Journal of Neuroscience Methods 182, 211–218 (2009).

Supplemental information

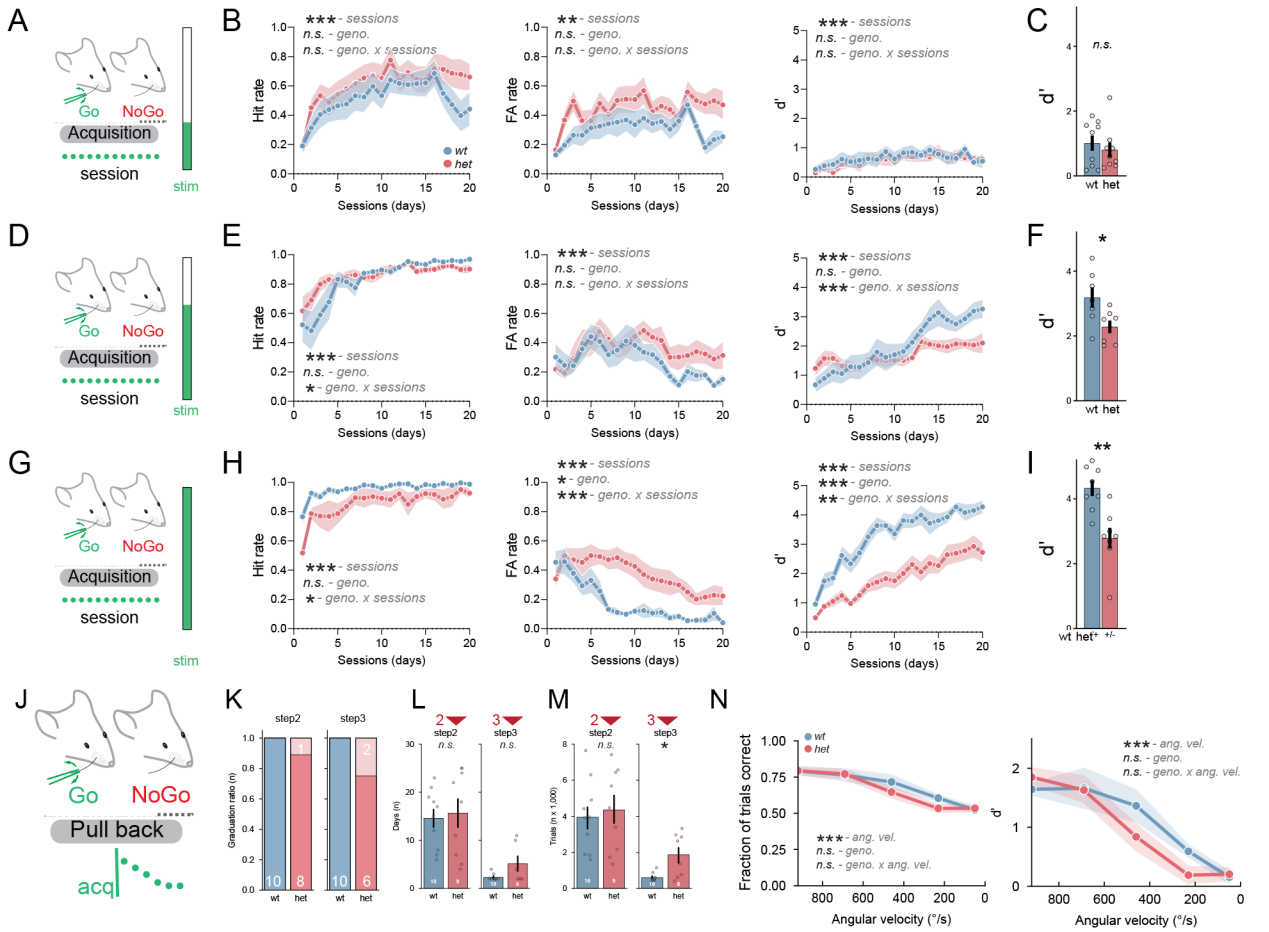

Figure S1. Additional measures during passive tactile stimulus (WDIL) in *Syngap1*$^{+/-}$ mice, related to Figure 1. Behavioral measures during WDIL training for the low (400 °/s) **(A-E)**, medium (650 °/s) **(F-J)** and high (900 °/s) **(K-O)** whisker stimulation corresponding to Figure1b. Hit/false alarm (FA) rates and d' scores during task acquisition are indicated for the three intensity levels **(B, E, H)**. d' scores after 20 days of acquisition for the 3 stimulus intensities **(C, F, I)**. **J-N.** Pull back experiments for the WDIL paradigm showing the ratio of mice graduating the task at the different step of training (step2 and step3) **(K)**, the number of sessions **(L)** and the total number of trials **(M)** to graduate step2 and step3 prior to the pull back experiment corresponding to Figure 1. **N.** Fraction of total trials correct) rate and d' score during decreasing whisker stimulation intensity of the pull back phase of the WDIL

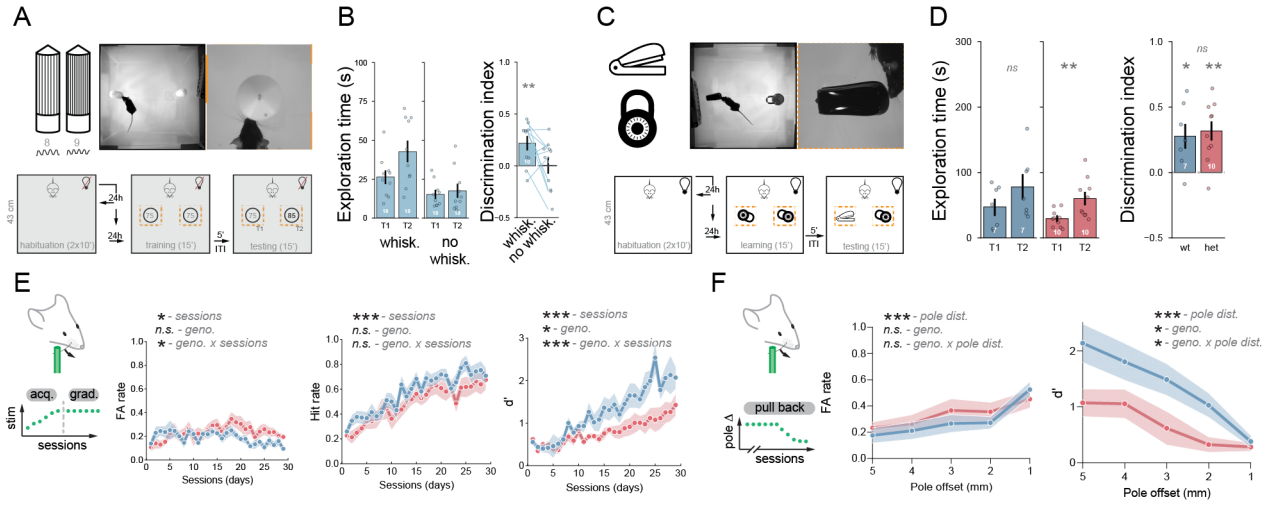

Figure S2. Additional measures for *Syngap1* role in active sensing paradigms related to Figure 2. A-B. Novel object recognition texture (NOR-T) task structure. Exploration time and discrimination index during the testing phase of the NOR-T for objects with 10 groves spacing difference **(A)** for wild-type animals performing the task with or without whiskers **(B)**. **C-D.** Traditional Novel Object Recognition (NOR) task structure **(C)**. Exploration time and discrimination index during the testing phase of the NOR for 2 different objects: a stapler and a lock **(D)**. **E-F.** Additional data for the whisker-dependent discrimination task during instrumental learning based on pole location for FA rate, Hit rate and d' during acquisition of the task (complementing Figure 2D-E) **(E)** and the pull back for FA rate and d' (complementing Figure 2F-G) **(F)**. (wt (blue) and *Syngap1*$^{+/-}$ (het, red); (n.s.: p>0.05, *: p<0.05, **: p<0.01, ***: p<0.001).

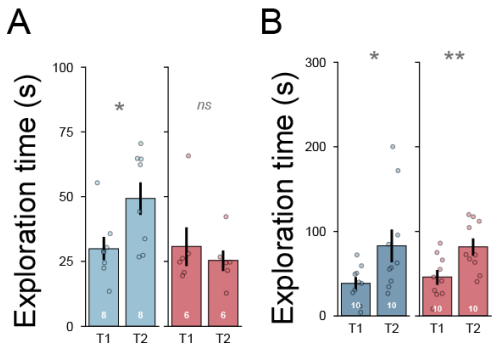

Figure S3 related to Figure 2. A-B. Exploration times during the testing phase of the NOR-T for objects with 10 groves difference (complementary to Figure 2b) and 25 groves difference (complementary to Figure 2c). (n.s.: p>0.05, *: p<0.05, **: p<0.01, ***: p<0.001).

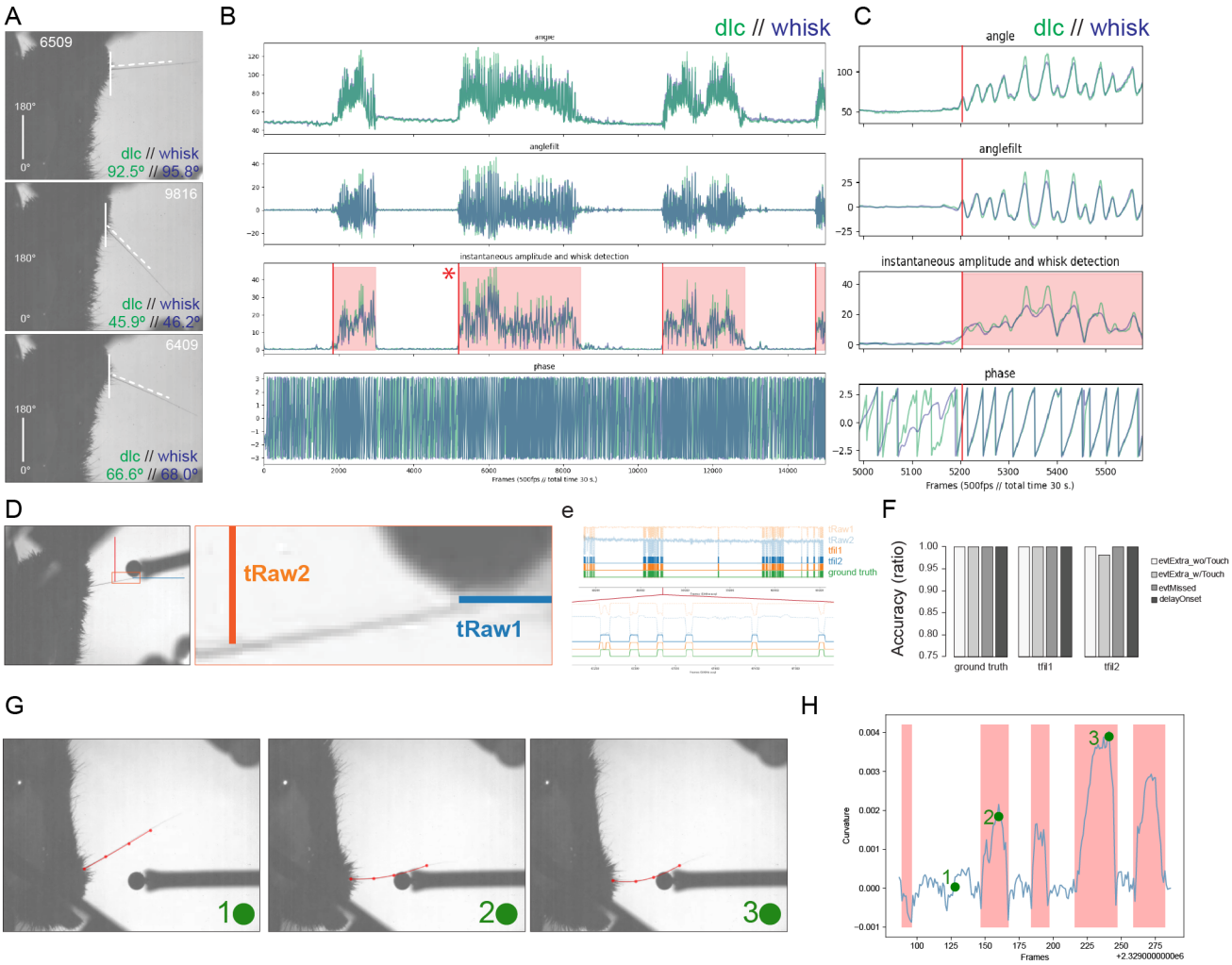

Figure S4 related to Figure 2. Whisker dynamics and touch detection analysis comparison between whisk and DLC. **A.** Screen shot of 3 random frames (frame number in white) from highspeed recordings. Raw angle obtained with DLC tracking of the whisker (green) and tracking with the whisk software (blue). **B-C.** Output of DLC and whisk for 4 different measurements (angle, filtered angle, instantaneous amplitude and phase) during a 30 seconds period (b) and a snippet of data at the red star for a duration of 1 second **(C)**. **D.** Example and validation of touch detection based on thresholding and DF/F of intensity when the whisker is within the tRaw1 and tRaw2 areas. **E-F.** Comparison of filtered signal with ground truth manually analyzed data **(E)** and their relative accuracy **(F)**. **G.** Example of curvature analysis with DLC fitting a polynomial onto the first 4 proximal whisker labeled points. Green dots are references to the frame equivalent to the curvature displayed in H. **H.** Curvature of the whisker over time with red boxes denoting the moment of touch detected as described in D.

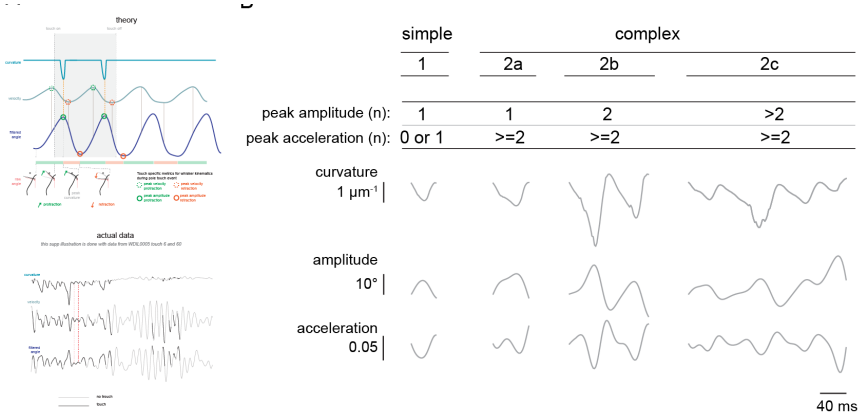

Figure S5 related to Figure2. A. Illustration theoretical and actual data whisker kinematics during whisking and touch against a pole in a head fixed freely whisking behavior. **B.** Illustration of the categorization of different types of touches, from simple to complex with the category 2c being the most complex observed.

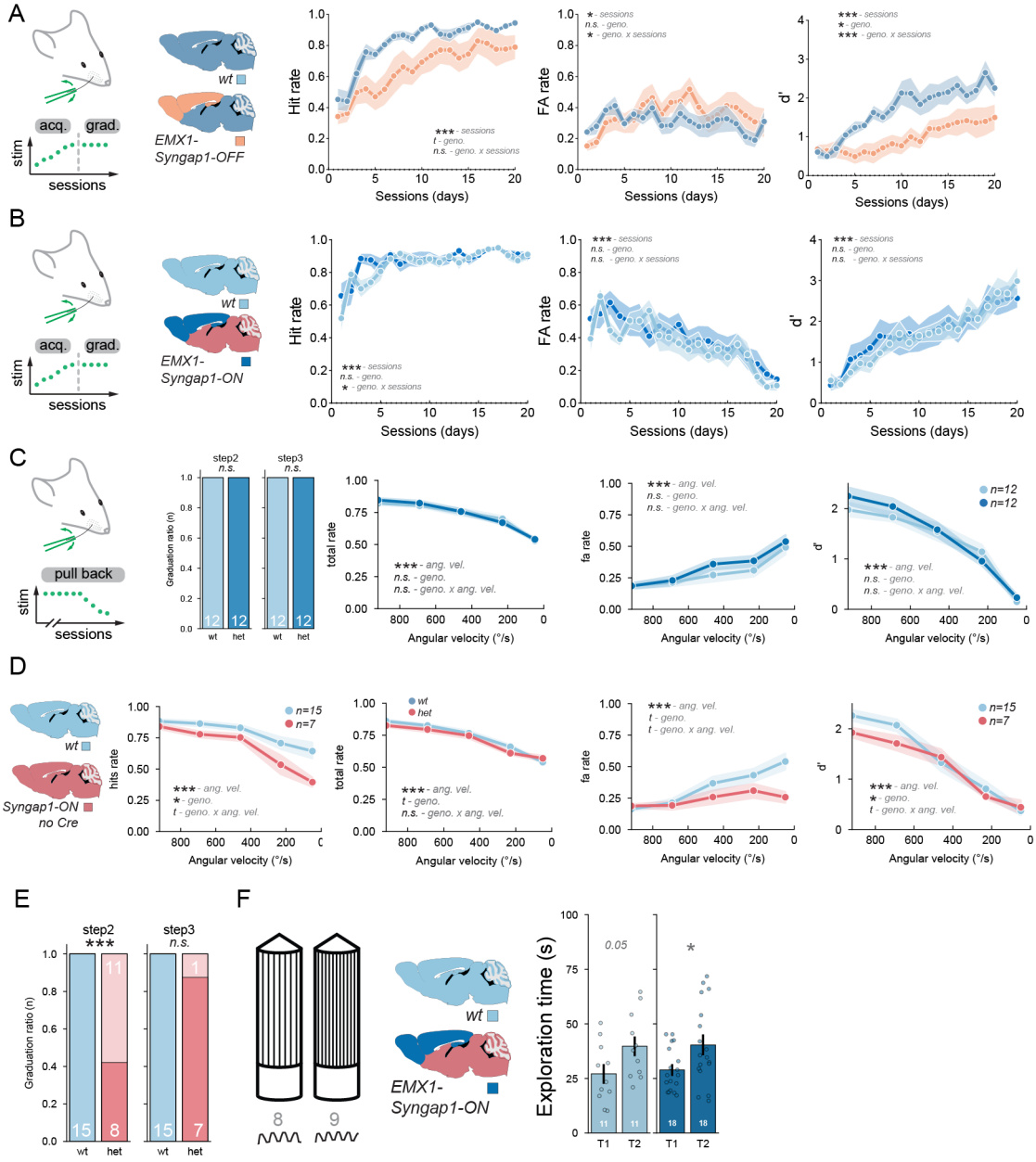

Figure S6. Additional measures for the modulation of *Syngap1* expression within cortical excitatory neurons during tactile sensitivity experiments related to Figure3. A. Hit/FA rates and d' during WDIL acquisition for wt and *EMX1-Syngap1-OFF* mouse line (complementary to Figure 3k). **B.** Hit/FA rates and d' during WDIL acquisition for wt and *EMX1-Syngap1-ON* mouse line (complementary to Figure 3L). **C-D**. Total fraction trials correct, FA rates and d' in *EMX1-Syngap1-ON* mouse line (complementary to Figure 3M) **(C)** and their genetic control counterpart which is not expressing Cre **(D)** during decreasing whisker stimulation intensity of the WDIL paradigm. **E.** Ratio of mice graduating the task at the different step of training (step2 and step3) for the genetic control counterpart of the *EMX1-Syngap1-ON* which is not expressing Cre. **F.** Exploration times during the testing phase of the NOR-T for objects with 10 groves spacing difference in *EMX1-Syngap1-ON* line (complementary to Figure 3N). (n.s.: p>0.05, *: p<0.05, **: p<0.01, ***: p<0.001)..

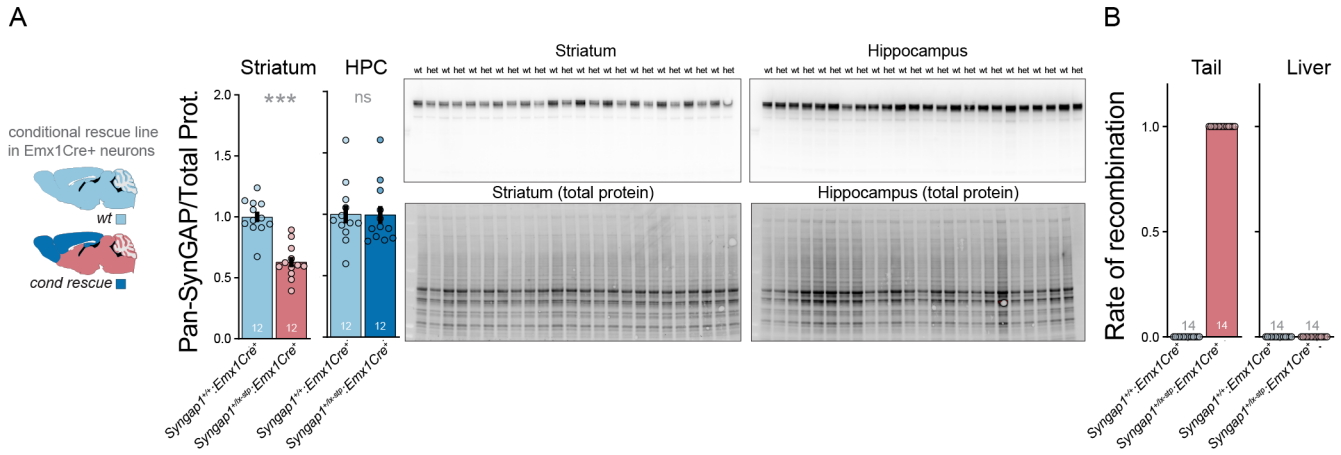

Figure S7 related to Figure 3. A. Immunoblots and quantification of Pan-SynGAP and total protein in the striatum and hippocampus from *EMX1-Syngap1-ON* mouse line. **B.** Rates of recombination in tail and liver tissue from *EMX1-Syngap1-ON* mouse line.

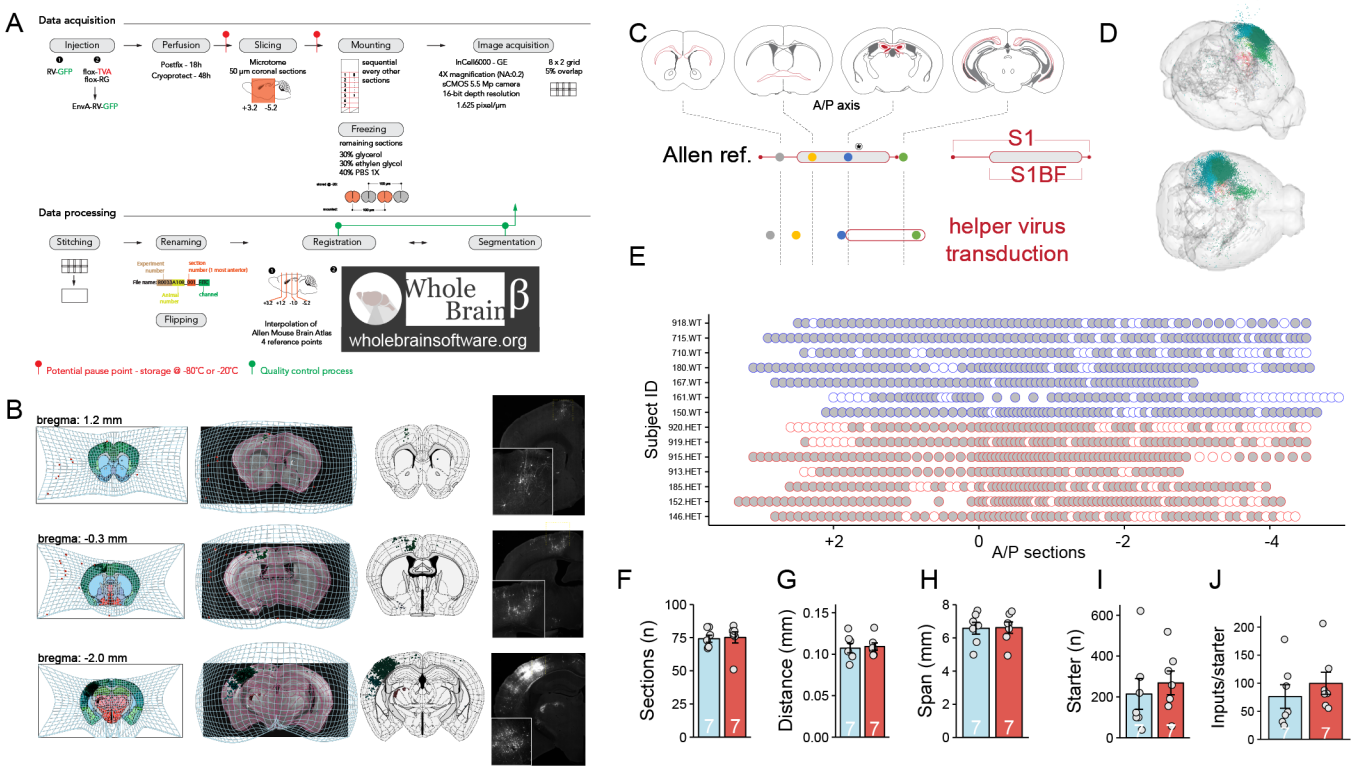

Figure S8 related to Figure 4. Experimental protocols related to rabies virus tracing and data associated with **Figure 5**. **A.** Experimental setup and timeline for data acquisition and processing of whole brain tracing data **B.** Cellular segmentation and registration using Wholebrain software for 3 representative coronal sections. **C.** Schematic representation of viral transduction. **D.** Example 3D brain of cellular registration from 2D coronal sections. **E.** Mapping of the distribution of the coronal section used for the analysis of all the samples in the antero-posterior stereotactic coordinates. **F.** Total number of sections in which cellular count and brain region registration was performed. **G-H**. Distance between every section sampled in the study **(G)** and their brain coverage **(H)**. **I.** Number of starter cells, cells expressing both GFP and mCherry in subsamples section. **J.** Ratio of the total number of inputs to the number of starter cells counted.

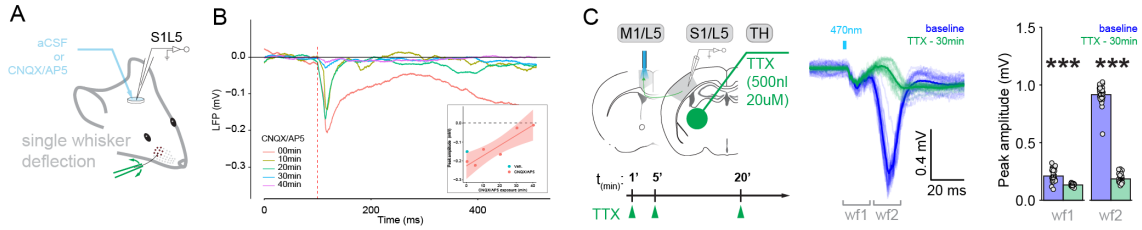

Figure S9. Afferent thalamocortical connectivity post whisker stimulation related to Figure 4. A. Cartoon representing recording of LFPs during single whisker deflection. **B.** LFP waveform and peak amplitude (inset) from wild-type mouse following application of CNQX and AP5. **c.** Cartoon representing recording of LFPs during optogenetic stimulation of M1 an thalamic application of TTX resulting in the quantification of baseline and TTX LFP responses in S1L5.

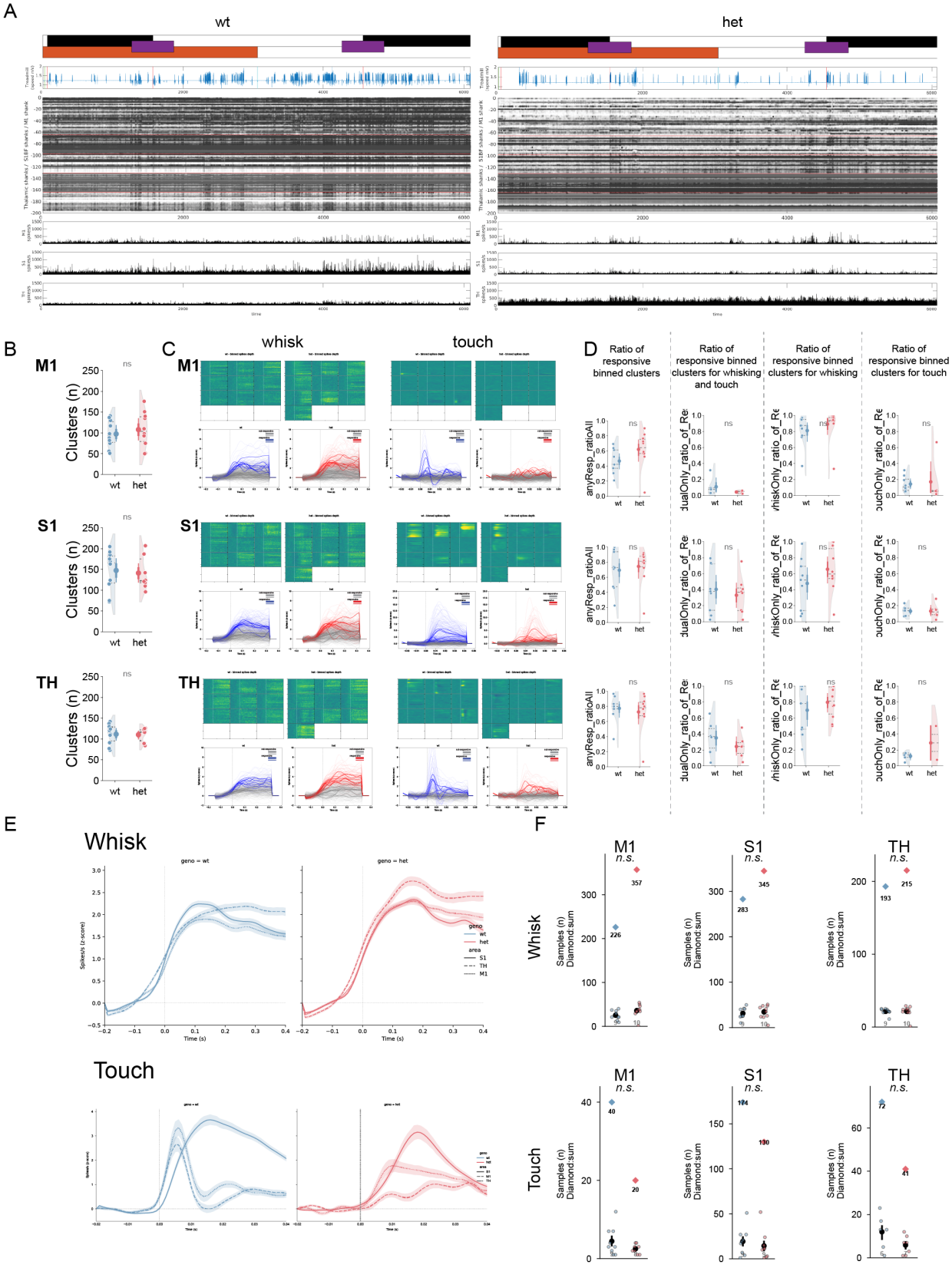

Figure S10. Multisite silicone probe recordings during behavior related to Figure 5. A. Representation of the environmental conditions present during the recordings (dark: black, light: white, pole present: purple, sound present: orange. Motion (blue trace) on the treadmill is displayed along with Drift map and spiking activities across M1, S1 and TH for 2 representative animals (wt and het). **B.** Number of clusters detected during the recording along the three areas per animals. **C.** Raster of the PSTH analysis by depth of the neuronal activity for M1, S1 and TH. Traces for responsive (colored) and non-responsive (grey) MUA clustered by depth are displayed for wt (blue) and het (red). **D.** Quantification of the ratio of responsive clusters and their proportion relative to being responsive only to touch, whisking or both whisking and touch. **E.** PSTH of whisking and touch responses across M1, S1, and TH. **F.** Number of samples represented per animals (circles) and the sum of all the responsive traces (diamond) for wt (blue) and het (red) mice. (wt (blue) and *Syngap1*$^{+/-}$ (het, red); (n.s.: p>0.05, *: p<0.05, **: p<0.01, ***: p<0.001).

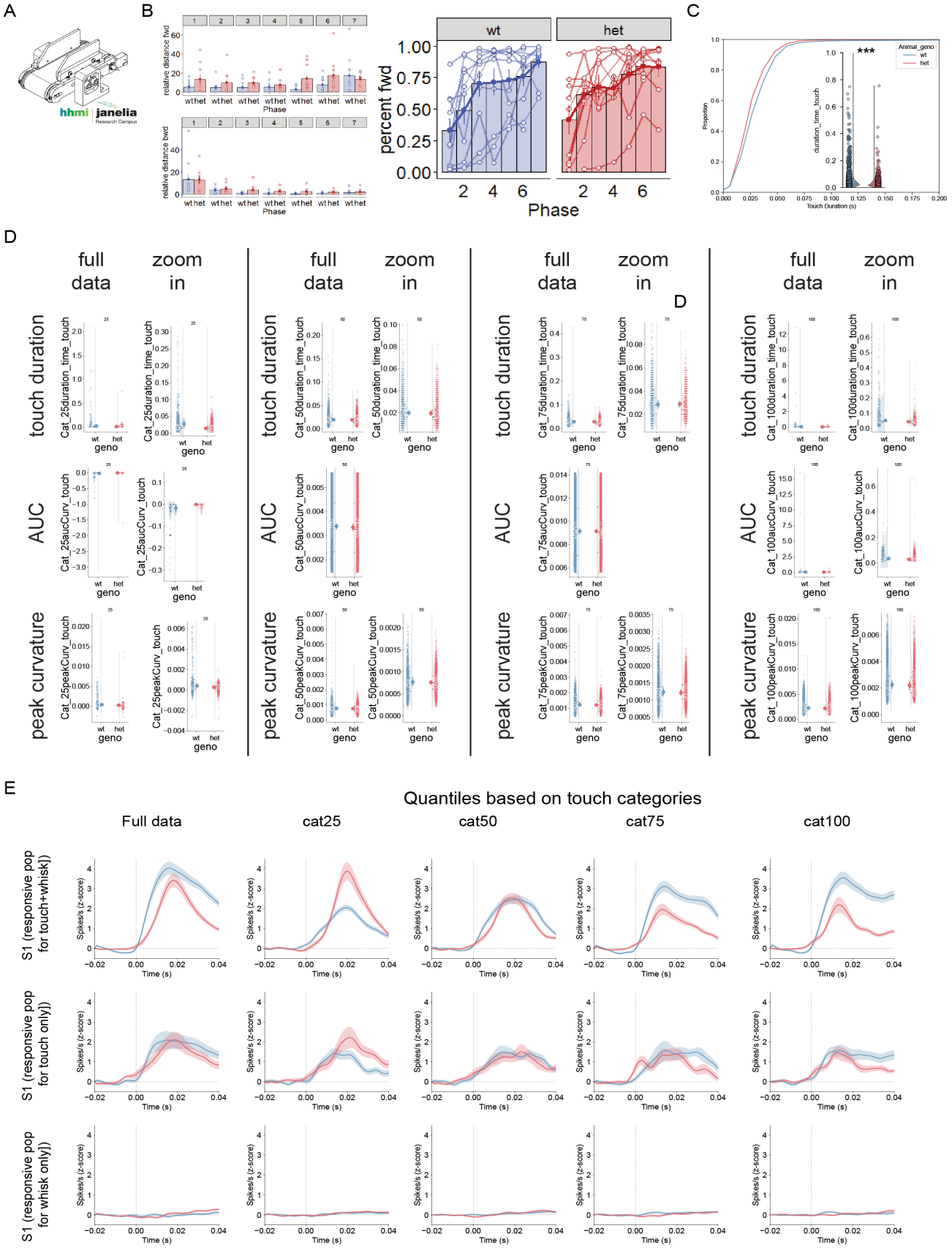

Figure S11 related to Figure 5. A-D. Behavioral metric during electrophysiological recordings. Illustration of the Janelia, Low Friction Rodent-Driven Belt Treadmill used during electrophysiology recordings **(A)**. Relative distance moved forward (top) and backward (bottom) during habituation for the first 6 days and recording (last day), the percent of forward movement during each phase of the experiment for wt and het mice **(B).** Cumulative distribution of touches in wt and het mice **(C). D.** Behavioral touch data which have been subdivided into 4 equal bins based on quartile of curvature and the corresponding measures: touch duration, AUC or peak curvature (rows) for each quartile are displayed. **e.** Classification of responsive population for whisking and touch behavior and their spike rates when subdivided by the curvature quartile described in d.

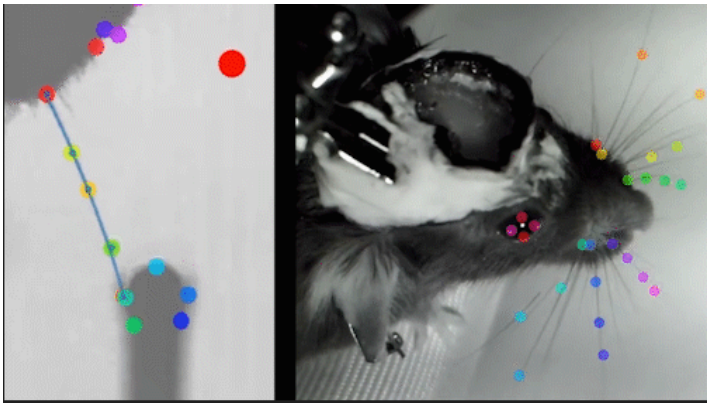

Video S1 (snapshot)

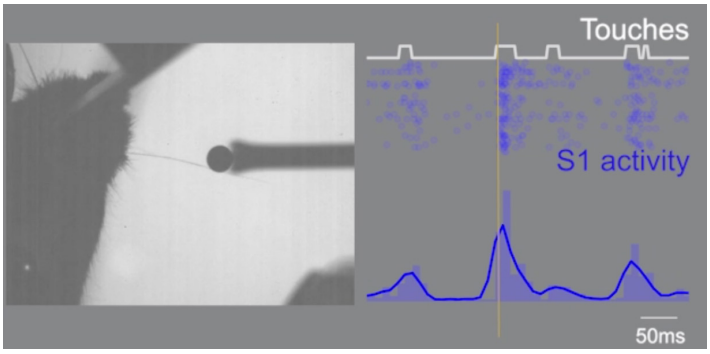

Video S5 (snapshot)

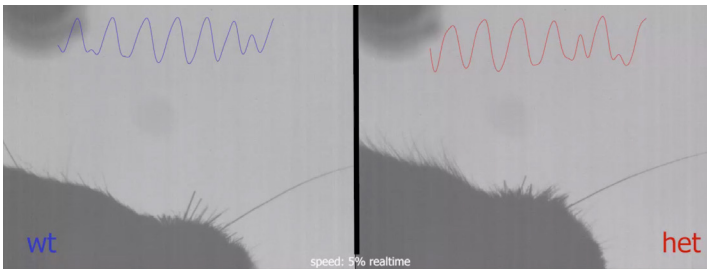

Video S2 (snapshot)

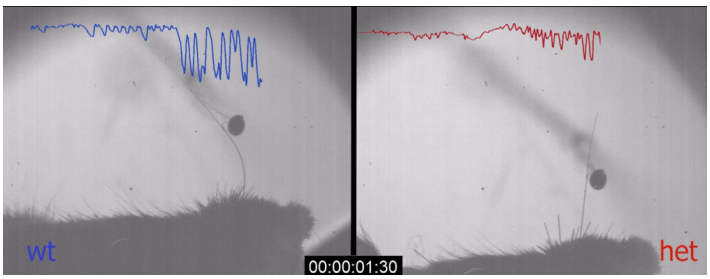

Video S3 (snapshot)

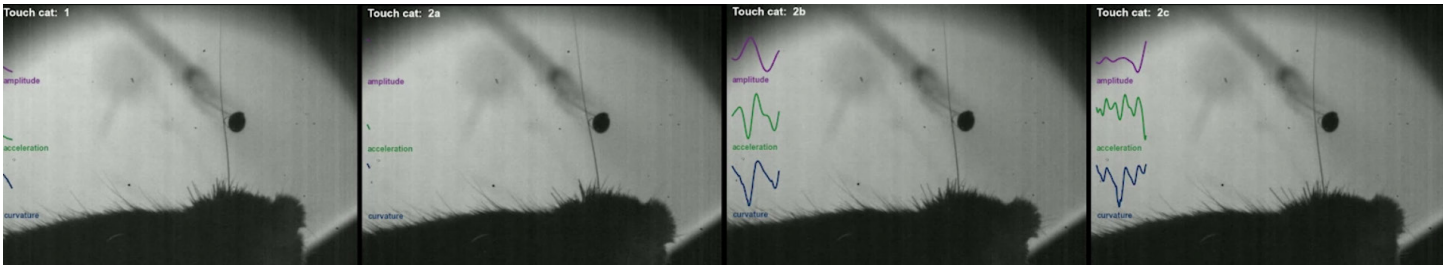

Video S4 (snapshot)

Methods

Mice

All mouse procedures were conducted in accordance with the NIH Guide for the Care and Use of Laboratory Animals, and all methods were authorized by the Scripps/UF Scripps Biomedical Research Institutional Animal Care and Use Committee. Both males and females (M/F) were used in all experiments except when explicitly noted. The design and maintenance of constitutive and conditional *Syngap1* lines have been described previously [66,91]. Briefly, we used inbred constitutive heterozygous *Syngap1* knock-out mice (*Syngap1*$^{+/-}$), conditional knock-out (*Syngap1*$^{+/fl,}$ JAX: #029303*)* and conditional rescue (*Syngap1*$^{lx\text{-}st}$ JAX: #029304) mouse lines. Emx1-Cre (JAX: #005628) mice were purchased form Jackson and crossed with *Syngap1*$^{+/fl}$ for conditional knock-out or *Syngap1*$^{lx\text{-}st}$ for conditional rescue experiments. Rbp4Cre mouse line (MMRRC_031125-UCD) was obtained from MMRC and was crossed to *Syngap1*$^{+/-}$ to study structural connectivity (monosynaptic tracing). Thy1-ChR2-YFP mouse line (JAX: #007612) was crossed to *Syngap1*$^{+/-}$ for functional validation and electrophysiological recordings. Cohort construction was designed to generate comparable sample sizes between genotypes and sexes, by allocating equal (if feasible) number of age-matched littermates from separate litters, usually more than two. Then, animals were assigned a number to hide the identity of genotype and/or group assignment. Experimentalists were blind to genotype at the time of data acquisition and analysis. Data collection occurred from mice >8 weeks of age. Mice were housed 4-5 per cage on a 12-hour normal light-dark cycle. In experiments requiring head-fixation, mice were transferred to a reverse light-dark cycle 2-3 weeks prior to headpost surgeries. Following headpost surgeries, animals were singly housed, with the addition of environmental enrichment in the form of a plastic running wheel (Bio-Serv) or a cardboard hut. Only animals that died, became non-responsive or did not participate in behavioral tasks during the study or data collection procedures were excluded from analysis.

Headpost surgery

Headpost surgeries were completed according to established procedures with minor modifications [23]. A custom titanium headpost was implanted onto the skull of 8-10 week old mice. Animals were anesthetized with isoflurane (5% induction, 1.5-2% maintenance) via a low-flow vaporizer (Somno Low-Flow Vaporizor, Kent Scientific) and placed into a stereotaxic frame (David Kopf Instruments). Body temperature was maintained at 37°C by a regulated pad with temperature feedback under the animal and ophthalmic ointment (Artificial Tears, Akorn) was placed onto the eyes for lubrication. The scalp was sterilized with alternating swabs of Betadine and 70 % ethanol. A small flap of skin was removed over the midline exposing both Lamda and Bregma, and the periosteum was gently cleared with a cotton swab. The skull was scraped with a scalpel and a thin layer of glue (Vetbond, 3M) was applied to the surface, reaching the wound margins. The headpost was lowered and affixed onto the skull via dental cement (Metabond, Parkell). Animals were injected (SubQ) with a cocktail of carprofen (10 mg/kg, Zoetis) and enrofloxacin (5 mg/kg, Norbrook), made in sterile saline (0.9 % NaCl, Vetivex). Animals recovered on a heating pad before being placed into their home cage. The same drug cocktail was injected once daily for the following two days for pain management and were routinely monitored for distress.

WDIL paradigm

Apparatus: The whisker dependent-instrumental learning (WDIL) paradigm was performed as previously described with minor modifications [23]. Briefly, mice were singly housed in a reverse light-dark room following headpost surgery and placed on water restriction (1 mL/d; food ad libitum), 3-7 days following recovery from headpost surgery. Animals were trained one session/day (~5d/week), all during the dark phase of the light cycle. The behavioral rig was controlled by BControl software (C. Brody, Princeton University) running in Matlab (2013B, Mathworks) on a master PC (Dell) and a Real-Time Linux State Machine (RTLSM). The behavioral rig consisted of a light and sound proofed box constructed from aluminum rails for the frame and black hardboard (Thorlabs) with sound attenuating foam. Head-fixation parts were custom built (Max Planck machine shop) and purchased from Thorlabs.

Habituation: Habituation to head-fixation commenced with handling of mice for 1 d, then presentation of a custom-built stainless steel body tube for 1 d. Mice were then exposed to head-fixation for 3 consecutive days with increasing time spent under head-fixation (10, 30 and 45 mins). Mice were continuously monitored via IR light and videography (Raspberry Pi HQ; Model 3B). White noise (70 dB) was continuously played within the apparatus and all subsequent sessions to attenuate room noise. Following habituation to head-fixation, all but one whisker on each side, C2, were trimmed under light (2%, isoflurane) anesthesia and kept trimmed throughout the experiment. The following day, mice learned to associate water availability by licking water from a lickport. Detection of licks was performed electronically[92] and precise water delivery (8 µL/ reward) was controlled with a solenoid valve and controller (INKA2424212H VHS-24V and IECX0501350A, The Lee Company). Lickport training lasted for a maximum of 10 mins/session or the total consumption of 1 mL of water per session (whichever came first), for two sessions. A lick would induce water delivery which could be consumed, however another lick would not deliver more water until a 1.5 s epoch passed. During lickport training, the C2 whisker was inserted into a plastic tube attached to a piezo to habituate the animals for training.

Training: Mice proceeded to WDIL training which was designed as a “detection” task, whereby the C2 whisker on the right side was plugged into the piezo actuator, acting as the Go signal and a “dummy” piezo was placed beside the whisker deflecting piezo but was not attached to a whisker, acting as the NoGo signal. Trials consisted of 50% “Go” and 50% catch (NoGo) trials in a random fashion, with the exception of no more than three consecutive trials could be of the same type. For Go trials, the whisker was deflected by the piezo actuator controlled by a linear voltage amplifier (E-650.00 and PL140.11, Physik Instrumente or EPA-008-1 – 1 and Q220-A4-203YB - 5+, Piezo.com) and a waveform generator (4054B, BK Precision), for 0.5 or 1.5 s (depending on the stimulus intensity) with a 40 Hz sinusoidal wave (rostral to caudal, 2-6 ° depending on the stimulus intensity). Bending of the piezo was calibrated using a laser-based displacement device (LD1610-0.5, Micro-Epsilon). For NoGo trials, the dummy piezo was stimulated in the same fashion as the whisker deflecting piezo, however no whisker stimulation was provided. The response window opened 0.1 s following stimulus onset and lasted for 2 s. During the response a window, a lick on the lickport resulted in a “hit” on Go trials and triggered an 8 µL water reward, and a “FA” on NoGo trials. Withholding a lick on Go trial resulted in a “Miss”, while no licking on NoGo trials resulted in a “correct rejection”. No water reward was provided on correct rejection trials and no punishments were given on Miss or FA trials. The intertrial interval remained constant at 4 s, but mice were required to withhold licking for 1.5 s before the piezo was stimulated for trials to proceed and therefore, provided some level of randomness of trial timing. Mice performed the task until satiated. Animals were trained for 20 consecutive sessions. Performance was based on a number of factors including total trials correct, discrimination index (d’; calculated as $d' = z(\text{hit}) - z(\text{FA})$, with z scores computed using the function NORMSINV in excel) and Hit and FA rates. Mice were scored to be expert learners (ie. reached learning criteria) when the following metrics were achieved for two consecutive days: d’ ≥ 1.1, total trials correct ≥ 70%, Hit rate ≥ 70% and FA rate ≤ 30%. Mice that reached criteria were graduated to a reduced stimulation protocol after 20 sessions that consisted of a similar task structure however, the stimulus intensity was reduced on consecutive days (6 °, 4.5 °, 3°, 1.5°, 0.5° for angular deflection).

NOR-T

Novel object recognition (NOR) and novel object texture discrimination (NOR-T) paradigms were developed for use with high-speed videography and conducted with *Syngap1*$^{lx\text{-}st}$ (heterozygous KO) and *Syngap1*$^{lx\text{-}st}$ x Emx1-Cre (conditional rescue) mouse lines to assess recognition memory

and whisker-dependent texture discrimination in a freely moving/non-head fixed behavioral setting as a proxy to assess somatosensory cortical function in these mice.

Apparatus: The apparatus was assembled using infrared-transmissible plexiglass sheets (Part # ACRY31430, ePlastics) to fashion an open-top box (44(L) x 44(W) x12(H) cm). Four infrared lamps were attached at each corner, a monochrome camera (A1300, Basler) with a 25mm lens positioned 56 cm over the center floor of the box and two high-speed cameras (Spark SP-5000M-CXP2, JAI) suspended 22 cm over each of the two objects were used for video recording. The Basler camera was set to record at 30 fps to assess full arena activity. The two high speed cameras were set to record at 160 fps to determine when and how long the mouse explored either object with its whiskers. The Basler camera video data was fed into Bonsai (https://bonsai-rx.org/) to track animals in real time and produce triggers in response to animals entering ROIs surrounding the objects. These triggers were fed, via an Arduino (Uno R3, Arduino), into the high-speed camera trigger to acquire frame captures. Video recordings from the high-speed cameras were recorded to a DVR system (DVR Express Core 2, IO Industries) using Coreview software for offline analysis.

NOR-T: 3D-printed white “cog-wheel” columns (7.4 (H) x 3 (D) cm) with different numbers of teeth (50, 75 or 85 per objects corresponding respectively to 5, 8 and 9 ribs/cm) with smoothed cone tops and a separate smooth-surfaced circular base (1.8 (H) x 3 (D) cm) into which the poles screwed served as objects for texture discrimination. Bases (equidistant from the corners and 9cm from each side of the arena) were fixed throughout the task while familiar (75-teeth) and novel (50 or 85-teeth) poles could be interchanged throughout the task for an entire cohort. Mice were run initially in two 10 min habituation sessions with no objects in the arena. The first session conducted with only the Basler camera suspended above the arena, and the second session conducted with all three cameras positioned as in the training and testing phases. On the following days, each mouse was run in a training session with two identical familiar poles and a testing session (15 mins each) with one of the familiar poles and a novel pole separated by a 5 min intertrial interval in the home cage. Poles were cleaned with 70% EtOH, dried, and stored in clean bedding between sessions while affixed bases were wiped cleaned and dried during ITIs with urine and fecal boli removed from the arena without additional cleaning. Arenas and poles were cleaned between animals. Positions of the novel pole were counterbalanced throughout the cohort. Overall activity was assessed during habituation phases. Time spent with familiar and novel poles were compiled using session videos analyzed manually with BORIS software (https://www.boris.unito.it/) by scoring the time when animal whiskers were in contact with the objects. Comparisons between training and testing phases were performed using two way ANOVA analyses, and % novel exploration ((novel time/(novel and familiar times) x 100) and discrimination index values ((novel-familiar times/(novel+familiar times) were calculated from the pole duration data for each mouse with genotype differences assessed with unpaired t-tests. Mice with at least 10 sec of cumulative pole exploration were included in statistical analyses.

NOR: Novel object recognition sessions commenced once all mice of a particular cohort finished NOR-T sessions and were conducted in the same manner as the NOR-T sessions with no initial habituation sessions. Two different types of objects (two identical master locks for the familiar objects and a mini stapler for the novel object) were used in this paradigm. These objects have been verified extensively as approachable with no significant biases for exploration time in the Frick lab [93] and in unpublished data from the lab. The objects were temporarily fixed to the floor of the arena with heavy duty double-sided tape not accessible to the mouse. Objects and arena were managed within and between training and testing phases as in the NOR-T paradigm including counterbalancing of the novel object position. Data were subjected to the same analyses as in the NOR-T paradigm. Mice with at least 30 sec of cumulative object exploration were included in statistical analyses.

Free-whisking and active touch paradigms

Following headpost surgery, habituation to head-fixation and whisker trimming (described above), whisker movements (C2 whisker on the left side) were recorded during “free-air” trials (no pole presented) in a dark, sound-isolated chamber while head-fixed. Videos (50 s in duration) were recorded at 500 Hz from above at 640 x 480 pixels resolution with a high-speed camera (DR1-D1312-200-G2, Photon Focus) coupled with a 0.243X bi-telecentric lens (MVTC23024, Thorlabs) and Streampix software (Version 8, Norpix). The field of view was illuminated from below with an array of infrared light-emitting diodes (B001BC52W2, Amazon) with a diffusion sheet (3026, Rosco) placed above the array.

For active touch experiments, a vertical metal pole (2 mm in diameter), was moved into the whisking range of the C2 whisker (left side) via a set of feedback controlled linear actuators (L16-P 50mm, Actuonix), controlled via an Arduino (Uno R3, Arduino) and a motor control board (Part # 1438, Adafruit). Placement of the pole was adjusted manually for each animal such that the pole resided in line with the snout (rostrally) and 5-8 mm lateral of the whisker pad. The pole was presented to the animals for a total of 5 mins each, however only the first 30 s following the first touch was used for further analysis.

Analysis of videos comprised of tracking whiskers offline using the Janelia Whisker Tracker [94], which supplied whisker traces in 2-dimensional space, followed by manual curation. Processing of this data was completed in MATLAB (2018b, Mathworks) using established protocols [95,96]. Briefly, instantaneous phase, amplitude and setpoint were acquired by using the Hilbert transformation of the band-pass (4-30 Hz, Butterworth) filtered angle. Instantaneous frequency was obtained from the derivative of the instantaneous phase following unwrapping and conversion to whisk cycle. Angular velocity and acceleration were quantified by taking the first and second derivatives of the smoothed (Savitzky-Golay filter; 3rd order, 9 frames) angle. Protraction and retraction values were resolved by obtaining positive and negative peaks of the resulting traces in question. The moment and duration of touch was determined manually via BORIS software by experimenters blinded to genotype.

Pole localization task

Mice were trained in a pole localization task (Go/NoGo), based on previous studies (O’Connor et al., 2010), in the same apparatus and with similar pre-training methods (surgery, water restriction, habituation, lickport training) described above for the WDIL paradigm with minor modifications. This task was designed as a “discrimination” task. Briefly, mice used the C2 whisker to discriminate between two pole locations. A smooth pole (1.6 mm in diameter) was positioned (8-12 mm lateral from midline) in a home position via a high resolution and repeatable stepper linear actuator (NA11B30-T4, Zaber) coupled to a low friction linear slide (6203K317, McMaster-Carr) prior to trial initiation. Mice were required to withhold any licking for 1.5 s prior to trial initiation for the trial to proceed. On Go trials, the pole was positioned in a posterior position (3 mm from home) and lifted into the whisker range by a pneumatic linear slide (SLS-10-15-P-A, Festo) attached to the linear actuator. On NoGo trials, the pole was moved to an anterior position (3 mm from home) and lifted. Therefore, the offset of the Go and NoGo was 6 mm, but adjusted for each animal so the home position was in line with the snout. It took ~500 ms for the pole to move into position and ~200 ms for the pole to move upward into whisker range. During this time, mice could lick the lickport without any effect on trial outcome. The response window started ~1 s after the start of the upward pole movement and was open for 2 s. Mice made their decision during this time by licking an electronic lickport. On Go trials, if the animal licked, they received an 8 µL water reward and was considered a hit. If they withheld their lick, it was considered a miss. On NoGo trials if the animal licked, it was considered a FA and the animal received a 15 s timeout with the pole remaining in the upward position. If they withheld their lick, it was considered a correct rejection, however no reward was provided. Following the end of the response window (and punishment time), the pole dropped and was moved back to the home position and a 4-6 s intertrial interval began. Animals performed 200-300 trials per session, 1 session/day, ~5 session/week for 29 sessions. Trial types (Go/NoGo) were presented randomly with the only limitation of no more than three of the same trial types could be presented in a row. Animal performance was quantified in a similar fashion to the WDIL paradigm described above.

High speed videography of mouse whiskers was performed on five sessions throughout the training, including Session 1, 17 and 25. These were picked to include whisking behavior when the animals were completely naïve to the task (HS1, session1), when the animals (at a population level) were well into the learning phase (HS3, session17), and at the end of training (HS5, session 25). An addition 2 sessions were recorded based upon individual learning curves. HS2 was performed for each animal when their learning curve showed a steep acceleration (session 10-15) indicating learning. HS4 was conducted after the animal had reached criterion for expert level (as described in the WDIL paradigm) for two consecutive days.

Acquisition of whisking behavior and pole touches during the task was performed using a high-speed camera (Spark SP-5000M-CXP2, JAI; ~500 Hz frame rate, 640 x 480 pixel resolution) under infrared illumination and recorded to a DVR system (DVR Express Core 2, IO Industries) using Coreview software. Each trial triggered a new recording that extended 3 s prior and 3.1 s after upward pole movement (using a pre-trigger buffer). This provided whisker activity prior to pole movement, sampling the pole and during decision making.

Whisker tracking and processing was performed using the Janelia Whisker Tracker and custom Matlab scripts, as described above, on a trial-by-trial basis. For whisking analysis during electrophysiological recordings whisker tracking was performed with DeepLabCut where 5 points along the single whisker track the whisker location. Whisker angle was calculated from the base of the whisker and the whisker pad to the next marker on the whisker. The moment of touch was quantified using a threshold-based method assessing the DF/F of pixel intensity within three 12x2 pixel areas 1 pixel away and tangential to the pole.

Monosynaptic tracing

Viral preparation and monosynaptic tracing were performed as previously described [73,75]. Monosynaptic inputs onto a genetically define cell population of Layer 5 neurons in S1 were targeted with helper virus AAV9-CAG-Flex-RG (Addgene 48333) and AAV9-CAG-Flex-TCB (Addgene 48332,[74]) in conjunction with pseudotyped rabies virus EnvA-RV-GFP in Rbp4Cre mouse line crossed with *Syngap1*$^{+/-}$. AAV9-CAG-Flex-RG (titer: 1.10^12 IU/ml) and AAV9-CAG-Flex-TCB (titer: 1.10^12 IU/ml) were mixed as a 1:1 ratio and 400 nl were unilaterally injected in S1BF (AP: -1.3 mm, ML:+3.0 mm and DV:-0.45 mm from Bregrma) at a rate of 200 nl/min. Two weeks after the first injection 400 nl of EnvA-RV-GFP (titer: 1.10^8 IU/ml) was injected in the same location at a rate of 200 nl/min. 7 days after injection of EnvA-RV-GFP the animals were deeply anesthetized and intracardially perfused with 0.1 M PBS followed by 4% paraformaldehyde.

Histology and image acquisition

After perfusion the brains were post fixed in 4% PFA overnight, placed in 30% sucrose for 3 days prior to being snap frozen in 2-methylbutane and stored at -80 °C. On the day of slicing the dorsal part of the brain was placed on a grid, aligned and subsequently embedded in OCT against a frozen razor blade at the posterior end of the brain, creating a plane perpendicular to the dorsal part of the brain and parallel to the microtome blade. This ensures the proper alignment of the brain in the medio/lateral and dorso/ventral axes which facilitates registration to the mouse reference atlas. The whole brain was sliced on a microtome at 50 um intervals, with every other slice mounted with DAPI (P36931, Invitrogen) onto a microscope slide. The brain was subsequently imaged on an INCell Analyzer 6000 (GE) for rapid acquisition with a Nikon 4X/0.20, Plan Apo, CFI/60 at 1.625 um pixel size. Acquired images were obtained using FITC (excitation: 488nm, emission: 525nm).

Quantification of monosynaptic tracing.

Retrograde labeled cell bodies were segmented and registered onto the mouse reference atlas using WholeBrain software [75]. To quantify the starter cell populations, sections with red signal from the transduction of AAV9-CAG-Flex-TCB were pre-identified and re-acquired on the InCell 6000 with a Nikon 10X/0.45, Plan Apo, CFI/60 at a resolution of 0.65 um pixel size for both FITC (excitation: 488nm, emission: 525nm) and dsRed (excitation: 561nm, emission: 605). The overlapping population of green and red cell bodies were manually quantified with ImageJ and defined as the starter cell population. All of the identified inputs for any given brain regions were normalized to the total number of starter cells identified per mouse brain.

Quantification of electrode tracks.

Sections were imaged on an IN Cell Analyzer 6000 (GE) with a Nikon 4X/0.20, Plan Apo, CFI/60 at 1.625 um pixel size with dsRed (excitation: 561nm, emission: 605) corresponding to the signal emitted by DiI to identify the electrode and FITC (excitation: 488nm, emission: 525nm) to capture the outline of the brain with autofluorescence of the tissue. The acquired images were stitched with channels merged prior to atlas registration and electrode track visualization, which was performed with SHARP-TRACK[97].

Electrophysiological Recordings

Mice went through a protocol to allow acquisition of electrophysiological recordings in multiple brain sites in an awake, head-fixed setting. Details of this protocol are detailed below.

Day1 - Surgery.

The mouse underwent headpost surgery, see prior Methods, with the following addition for electrophysiological recordings. The entire scalp was removed and the periosteum was gently cleared with a cotton swab. The skull was then leveled in the antero-posterior axis by having Bregma and Lambda in the same plane, while the medio-lateral axis was leveled by adjusting the lateral point in the same plane 2 mm from the midline on each side. Enough bone was shaved from the skull with a 0.6 mm drill bit to create four reference points. This procedure did not result in exposing the brain. The reference points were located above the future electrode point of entry to reach the motor cortex (M1; AP:1.0, ML:-1), the thalamus (TH, AP:-1.5, ML:-1) and the somatosensory cortex (S1, AP: -2, ML: -3.5), along with the front left corner where the headpost would be located (AP: -5.5, ML: 1.5). A silver wire pre-soldered to a female gold pin was in contact with the brain above the cerebellum (AP:-5.5, ML:0). Dental cement (Metabond, Parkell) was applied to secure the 3D printed plastic well, headpost and ground wire. At the end of the procedure Kwik-Cast (World Precision Instruments) was applied within the well to protect the skull surface for downstream procedures.

Day4 - IOS imaging.

Three days after recovery of the headpost surgery, Intrinsic Optical Imaging (IOS) was performed to measure the hemodynamic response of the somatosensory cortex to define the cortical area corresponding to brain activity responses after single whisker stimulation (C2). The mouse was anesthetized as described in the headpost surgery protocol. All the whiskers were fully trimmed to the base of the whisker pad except for the whisker C2 contralateral to the cortical area of interest (trimmed to a ~5 mm length). The skull was drilled in concentric circles over S1 (AP: -2, ML: -3.5) through the spongy bone. Debris were removed with compressed air and Ringers solution was applied to cool the bone and remove the debris. When cerebral blood vessels became visible a scalpel blade (#501251, World Precision Instruments) was used to shave the bone further until blood vessels were clearly visible. The mouse was moved from the stereotaxic instrument to the IOS imaging rig and the anesthesia was reduced to 0.7% in conjunction with the injection of a sedative (chlorprothixene; 1 mg/kg, intramuscular). Kwik-Cast was removed from the well and ophthalmic ointment (Artificial Tears, Akorn) was applied on the edge of the well filled with saline and sealed with a glass coverslip. IOS imaging was subsequently performed as previously described[23]. Briefly, imaging was performed under a 4x objective on an upright microscope (BW51X, Olympus) and the skull was illuminated with a 630 nm LED light ring mounted to the objective. Images were acquired with a Zeiss Axiocam camera (Carl Zeiss) controlled my µManager software (Open Imaging, Inc.). The C2 whisker was deflected for each IOS trial (50-70 trials total) and

resulting images were processed using the IO and VSD Signal Processor plugin in ImageJ [98].

Day5-11 - Habituation. The day after IOS imaging, the mouse was habituated to head-fixation on a treadmill (https://www.janelia.org/open-science/low-friction-rodent-driven-belt-treadmill). The mouse was handled for 5 min in the morning. In the afternoon it was handled for 5 min prior to being introduced to the treadmill and allowed to explore the treadmill for 5 min. Day 6 was the first day of gradual head fixation with the animals being head-fixed for 15 min, 30 min on day 7, 1hr on day 8 and day 9, and finally 2hr on day 10 and 11.

Day12 – Surgery.

The mouse was placed in the stereotaxic apparatus (KOPF) to perform 3 craniotomies for future electrode insertion. The C2 whiskers was trimmed to a length of 5 mm. The skull was properly positioned (correction for antero/posterior and medio/lateral tilt). Circular craniotomies of a 1.5mm diameter were drilled automatically with the Neurostar surgery robot with a 0.2 mm drill bit (Harvey tool) above the area marked during the head-post surgery and identified with IOS for the S1 craniotomy. Once the drilling was performed, the inner part of the bone was removed. Gelfoam and Ringers solution were applied to minimize potential bleeding. Kwikcast was applied to protect the brain after the craniotomy and the mouse was placed on a heating pad for recovery before returning to its home cage for 3 to 4 hrs.

Day12 – Apparatus.

The apparatus was a 30 inx30 inx50 in custom made noise-attenuated chamber mounted on a breadboard (MB30, Thorlabs). The recording consisted of a 20 min period in the dark followed by 40 min in the light and 20 min in the dark. In the middle of this sequence white noise that was playing (70 dB) was turned off. In addition, 2 pole presentation epochs of 10 min occurred 5 min prior to the light transition. Light, white noise, and actuators (L16-P 50mm, Actuonix) for the pole presentation were controlled via Matlab through a NI DAQ (USB-6363).The signals for the NI DAQ converged to the eCuber Server (White Matter) for synchronization. The mouse was video monitored with e3Vision Cameras (White Matter). Mouse whisking and touch behaviors were acquired at 500 Hz with a high-speed video camera (DR1-D1312-200-G2, Photon Focus) and a variable zoom lens (Computar) with StreamPix 6.0 software for the entire duration of the recording. The high speed captured video was downsampled with ffmpeg software (Version 4.0.2) before data analysis. IR light illuminated the mouse and a custom IR backlight was located underneath the mouse during video recording. Three 3-axis micromanipulators (New Scale Technologies) were mounted on an inverted 360 MPM-1 platform (New Scale Technologies) to enable probe insertion at 3 different locations. H2 probes for TH, H2 or H3 probes for S1 and H3 probes for M1(Cambridge Neurotech) were connected via Molex, Omnetix connector adaptor to the HS64 head stages (White Matter), which were connected to the e3 Server (White Matter). The fully retracted probes were positioned in the insertion probe axes above predetermined stereotaxic coordinates of the area of interest. Prior to placement on the manipulators the probes were coated with DiI (Life Technologies, #V22885).

Day12 – Data acquisition.

The mouse was placed on the treadmill and moved to the rig for probe insertion and recording. The reference and the grounds of the probes were grounded to a common ground shared with the ground of the animals. After the mouse was placed in the recording apparatus all the probes were manually lowered to a few millimeters above the skull surface. The position of the probes was monitored with a digital microscope (Dino-Lite, Premier) and the S1 probe was refined based on the blood vessel map corresponding to the responsive area of whisker stimulation determined by IOS imaging. The probes were then lowed at coarse intervals with the manipulator to break the dura. When all the probes were implanted, the probes were further inserted automatically at a rate of 200 um/min until the pre-determined target depth was reached. The probes settled for 30 min prior to recording. Electrophysiological data were acquired at 25 kHz using the Open Ephys GUI with the e3 custom module. Binaries were acquired along with digital and analog data streams from the NI DAQ box through the E3 servers. Whisking and touch behavior were acquired at 500 Hz. At the end of the recording the probes were removed and cleaned and immersed in 1 % Tergazyme overnight.

Data Analysis – Electrophysiology.

Raw binaries were processed in Matlab (2018). Median noise filtering was applied and channels were sorted according to the channel map, followed by common average referencing. From the binaries, action potentials (APs) and local field potentials (LFPs) were extracted using a Butterworth low pass filter between 0.5 and 100 Hz for the LFPs and a high pass filter between 300 Hz and 6kHz for the APs. The filtered APs were run through spike sorting software (Kilosort 2.0). Clusters of spikes were identified as “good” isolated units and “multi-unit activity”. Spike times for these categories were assigned to a specific depth in order to obtain a measure of overall spiking at a given location. Whisking onset was defined when the whisking amplitude increased by 2° within a 250 ms period [78]. The epochs during which the pole was present were excluded from the whisking analysis. Spike rate was aligned to the whishing onset to obtain peri-stimulus time histograms (PSTH) based on depth of the probes. The PSTH for whisking were performed with analysis window from -0.25 to 0.5 s and a baseline from -0.25 to 0 s with bins of 10 ms. The touch onset was identified with a threshold-based method registering whisker and pole interaction. Manual validation of the method was performed on a subset of the data. The pole was position was maintained between both pole presentations and kept relatively standard between animals via following the position of a guided template overlay on the live camera view. The whisker resting state was posterior to the pole and any touch occurring when the whisker was anterior to the pole was removed from the analysis. PSTH analysis for touch was performed similarly to the whisker’s PSTH with 1 ms bins, an analysis widow from -0.025 to 0.05 s and a baseline from -0.025 to 0 s. The z-scored PSTH for whisking and touch were smoothed with a Gaussian kernel using the smooth function. Artifacts at the end and beginning of the traces were removed from the analysis. Responsive clusters by depth were defined as z-score firing rate above 1.5 in the post baseline window. The Findpeak function was used to identify the peak value of the trace crossing this threshold and onset of the response was defined as the first inflection point of the trace from the identified peak to the beginning of the trace.

In vivo single electrode field recordings

LFP recordings were made on a custom in vivo system as described previously[23]. Briefly, mice were anesthetized with 1.8 g/kg urethane (Sigma-Aldrich), followed by implantation of a custom headplate, and a 1 mm craniotomy was made over S1. The pipette was lowered 500 µm from the brain surface in S1 (AP: 3.5, ML: 2). Recordings were performed in current-clamp mode with the following internal solution in the electrode (mM): 130 potassium gluconate, 5 KCl, 10 HEPES, 10 sodium phosphocreatine, 0.4 EGTA, 1 Na-GTP and 4 Mg-ATP (pH 7.3, 285-290 mOsm). Electrophysiological signals were amplified with Multiclamp 700B (Molecular Devices), filtered at 2 KHz, digitized (10 KHz) with an NI USB-6363 DAQ (National Instruments) and recorded using the NI acquisition system in Matlab. Optogenetic stimulation was controlled via the NI acquisition system in Matlab and relayed through the NI DAQ, a LED controller (LEDD1B, Thorlabs), fiber optic LED 470nm (M470F3, Thorlabs) and a fiber optic cannula (CFML12L02, Thorlabs) inserted in M1 (AP:1.0, ML:-1, DV:-0.5). Before each experiment the power of the laser was calibrated to obtain the following powers 1, 5, 10, 15, 20, 25,30, 35 and 40 mW/mm2 at the end of the fiber optic. Piezo stimulations were performed on a single whisker with a deflection of 200 µm at 2 mm away from the whisker pad (6° or 1200 °/s). To obtain LFPs, 30 trials were averaged.

Statistics

Data analyses were conducted in GraphPad Prism (version 9.4.1, GraphPad Software) or custom Python scripts (version 3.9). Linear mixed models with repeated measures were used in passive and active WDIL experiments to determine differences in overall genotype performances and their learning differences within these tasks by assessing interactions between genotype and session progression during acquisition phases or an-

gular velocity degression during “pullback” phases. ANOVAs and t tests were utilized to compare genotype differences within, between, or among different categories or stages of WDIL experiments, as well as NOR/T experiments, whisker kinematics comparisons, synaptic/circuit connectivity experiments and brain region-specific neural activity experiments. Kaplan-Meier survival curves were utilized to compare genotype differences in reaching endpoints, namely, reaching criteria for a particular stage of a WDIL task. Data are presented as mean ± SEM unless otherwise noted. D’Agostino-Pearson omnibus normality test was applied to test data normality and the appropriate parametric or non-parametric statistical test was performed accordingly. The statistical tests used and number of observations are reported explicitly in a comprehensive table **(Table S1)**. *P*-values are corrected for multiple comparisons when multiple simultaneously statistical comparisons were performed. No statistical test was used to predetermine sample sizes, however, our sample sizes are similar to those previously reported in the field [23,78].

Table S1 - zoom in to access content